

Eulerian-Lagrangian simulations of shear-thinning and shear-thickening in suspensions of repulsive particles

Carl Dahmén,¹ Christopher Ness,² and Luca Mazzei^{1, a)}

¹⁾Department of Chemical Engineering, University College London, Torrington Place, London WC1E 7JE, UK.

²⁾School of Engineering, The University of Edinburgh, King's Buildings, Edinburgh EH9 3FG, UK.

(Dated: 14 October 2024)

Repulsive non-Brownian particles dispersed in Newtonian fluids give rise to a complex rheology, shear-thinning at low shear rates and shear-thickening at high shear rates. Although these suspensions have been extensively investigated, the microscopic mechanisms underlying their rheology remain in part unclear. In this work, we develop a numerical Eulerian-Lagrangian model to describe the dynamics of neutrally buoyant, non-Brownian, repulsive particles dispersed in a Newtonian fluid and use the model to study and characterize the rheology of the suspension in a pure shear flow. Using a simple force balance and accounting for the drag-force hindrance function in the nondimensionalization of the shear rate, we retrieve the onset of shear-thickening at the expected order of magnitude of the dimensionless shear rate. Furthermore, we derive a modified Krieger-Dougherty equation that correctly predicts the rate of shear thinning. This equation highlights the importance of the relationship between the jamming volume fraction and the shear rate. Finally, we show how the jamming volume fraction is related to the shear-thinning and shear-thickening behaviors, linking it to the suspension microstructure.

I. INTRODUCTION

Suspensions of non-Brownian electrostatically-repulsive particles demonstrate a complex rheology characterized by shear-thinning, shear-thickening, and regions where the viscosity does not depend on the shear rate. The repulsive inter-particle forces, or *electrostatic double layer forces*, arise from ions that accumulate around the particle surfaces and form electric double layers resulting in forces that decrease exponentially with distance from the particle surfaces. The magnitude and characteristic range (*Debye length*) of these forces depend on material properties and ionic strength and affect significantly the viscosity of the fluid-particle suspension; for instance, Jeffrey and Acrivos^[1] observed that increasing the ionic strength reduces the viscosity by orders of magnitude. In numerous processes, controlling the suspension ionic strength and pH is crucial for achieving the desired performance, because this is closely related to the rheology of the fluid-particle suspensions, and in particular to the value of the viscosity. For instance, in the coating of catalytic converters², maintaining a low viscosity of the “washcoat” is critical.

Viscosity is correlated with solid volume fraction, strength and range of ionic forces, and shear rate. Establishing this functional dependence would greatly facilitate process design and optimization. To achieve this, one must model the dynamics of the fluid-particle suspension, accounting for the ionic forces, and extract rheological information via averaging³. Here, the only modeling approach that is suitable is the one that models the dynamics of each individual particle, because it permits to accurately capture all relevant particle-particle interactions, including those arising from repulsive forces. On

the other hand, a detailed description of the fluid dynamics of the ambient fluid, at a length scale much smaller than the size of the particles, is unnecessary; here, a mean-field description suffices, where the fluid-particle interactions are modeled via appropriate closures. This leads to the unresolved Eulerian-Lagrangian modeling approach adopted in this work⁴. This approach does not yield the suspension rheology directly; to find information about the rheology, one must determine the stress tensor of the suspension. To this end, one must employ a suitable averaging scheme – the same scheme used for modeling the solid phase as a continuum, which leads to the Eulerian-Eulerian description of the mixture dynamics⁵.

Suspension rheology is a broad and rich research field that has benefited from much recent progress, particularly in coupling the physics at the particle scale to the rheology at the macroscopic scale⁶. An important characteristic of suspensions is the *jamming transition*, where suspensions that could flow at a low solid volume fraction become solid at a critical or *jamming solid volume fraction*. This threshold value is important, because suspension rheology strongly depends on how far the solid volume fraction is from it⁷, the most common relationship between solid volume fraction and suspension viscosity being the Krieger-Dougherty equation⁸. The jamming transition is sensitive to various particle properties, such as friction⁹, particle shape¹⁰ and adhesion¹¹. A key finding is that the jamming phenomenon results from the network of particle contacts that is established under shear conditions¹².

We have developed a Computational Fluid Dynamics - Discrete Element Model (CFD-DEM) code based on “CFDEM”, an open source CFD-DEM framework¹³. The CFD part of this model includes the locally-averaged mass and linear momentum balance equations for the fluid phase and thus calculates (instead of assuming) the locally-averaged velocity and shear rate fields of the fluid phase and in turn of the suspension. Accounting for the local dynamics of the fluid phase rather than assuming it and considering only the particle dynamics

^{a)}Author to whom correspondence should be addressed;
electronic mail: l.mazzei@ucl.ac.uk.

(that is, the DEM part of the model, as done in e.g. Ness and Sun^[14] and Mari *et al.*^[15]) renders the model more accurate, because it allows capturing inhomogeneities in the velocity and shear rate fields.

This work aims to establish the dependence of the viscosity of suspensions of repulsive particles on the shear rate and solid volume fraction, paying particular attention to the jamming volume fraction. We focus on suspensions of neutrally buoyant particles, assuming that the Stokes number related to the mean velocity fields of the fluid and solid phases is much smaller than unity. These assumptions are important, because if they are not met, the suspension cannot be modeled as an effective fluid and the concept of suspension viscosity loses its meaning.

The article is organized as follows. Section II introduces the Eulerian-Lagrangian model used to simulate the suspension. In Section III, we present the equations of closure and subsequently the Eulerian-Eulerian and mixture models used to define the suspension properties, and in particular the effective stress tensor of the mixture and the mixture viscosity. In Section IV, we present the simulation parameters and briefly discuss the numerical stability aspects. Section V investigates the physical mechanisms underlying the rheology of suspensions of repulsive particles, deriving a modified Krieger-Dougherty equation. Section VI presents and discusses the simulations and the jamming volume fraction associated with suspensions of repulsive particles of different Debye lengths. In Section VII, we conclude the presentation of the results. The paper includes two appendices. In Appendix A, we derive a new critical time step for overdamped systems, and in Appendix B, we derive the scale of the drag force that accounts for the hindrance function.

II. MODEL

In this section, we introduce the Eulerian-Lagrangian model employed for simulating the suspensions. Note that the variables are locally defined, being functions of the spatial position \mathbf{x} and of the time t . Often, for convenience, these dependencies are omitted.

A. Locally-averaged equations of motion for the fluid phase

The Eulerian equations of motion for the fluid read:

$$\partial_t(\varepsilon\rho_e) = -\partial_{\mathbf{x}} \cdot (\varepsilon\rho_e \langle \mathbf{u} \rangle_e) \quad (1)$$

$$\begin{aligned} \partial_t(\varepsilon\rho_e \langle \mathbf{u} \rangle_e) &= -\partial_{\mathbf{x}} \cdot (\varepsilon\rho_e \langle \mathbf{u} \rangle_e \langle \mathbf{u} \rangle_e) \\ &\quad - \partial_{\mathbf{x}} \cdot \langle \mathbf{S} \rangle_e + \varepsilon\rho_e \mathbf{g} - n \langle \mathbf{f} \rangle_p \end{aligned} \quad (2)$$

where ρ_e and ε are the density and volume fraction of the fluid, respectively. The angle brackets denote a volume averaged property. $\langle \mathbf{u} \rangle_e$ is the mean fluid velocity, $\langle \mathbf{S} \rangle_e$ is the fluid effective stress tensor, \mathbf{g} is the gravitational field, n is the particle number density and $n \langle \mathbf{f} \rangle_p$ is the force exerted

by the fluid on the particles per unit volume of suspension.

The expression of the fluid effective stress tensor was derived, through a rigorous averaging procedure, by Jackson^[3], and reads:

$$\langle \mathbf{S} \rangle_e \equiv \varepsilon \langle \boldsymbol{\sigma} \rangle_e + n \langle \mathbf{A} \rangle_p + \varepsilon \rho_e \langle \hat{\mathbf{u}} \hat{\mathbf{u}} \rangle_e \quad (3)$$

where $\langle \boldsymbol{\sigma} \rangle_e$ is the mean value of the point stress tensor of the fluid and $\langle \hat{\mathbf{u}} \hat{\mathbf{u}} \rangle_e$ is the mean value of the dyadic product of the fluid velocity fluctuations. The first term on the right-hand side of Eq. 3 is present because, before the averaging is carried out, the liquid phase is already a fluid and consequently is already endowed with a point stress tensor. The last term on the right-hand side of Eq. 3 is a Reynolds stress type of contribution but not necessarily turbulence-related. The term $n \langle \mathbf{A} \rangle_p$ is related to the fluid dynamic interaction between the fluid and the particles (through the traction forces exerted by the fluid on the surfaces of the particles) and is referred to as particle-presence stress tensor; see Jamshidi, Angeli, and Mazzei^[16] and Jamshidi *et al.*^[17] for further details. We repartition this tensor in two parts, writing:

$$n \langle \mathbf{A} \rangle_p = n \langle \mathbf{A} \rangle_p^* + n \langle \mathbf{A} \rangle_p^\bullet \quad (4)$$

The starred term is related to the distortion of the fluid streamlines around the particles; this term is always present, also in dilute suspensions, where it yields the Einstein correction for the mixture viscosity³. The other term accounts for the lubrication films; this term becomes important in dense suspensions¹⁷. Now, if we define:

$$\langle \mathbf{S} \rangle_e^* \equiv \varepsilon \langle \boldsymbol{\sigma} \rangle_e + n \langle \mathbf{A} \rangle_p^* + \varepsilon \rho_e \langle \hat{\mathbf{u}} \hat{\mathbf{u}} \rangle_e \quad (5)$$

we obtain:

$$\langle \mathbf{S} \rangle_e = \langle \mathbf{S} \rangle_e^* + n \langle \mathbf{A} \rangle_p^\bullet \quad (6)$$

The first term on the right is always present, while the second term is significant only in dense suspensions.

B. Equations of motion for the solid particles

The equations of motion for each individual particle of the solid phase read:

$$m \ddot{\mathbf{u}}_r = \mathbf{f}_r + \sum_s (\mathbf{f}_{rs}^c + \mathbf{f}_{rs}^i) + m \mathbf{g} \quad (7)$$

$$I \ddot{\mathbf{w}}_r = \mathbf{l}_r + \sum_s (\mathbf{l}_{rs}^c + \mathbf{l}_{rs}^\bullet) \quad (8)$$

where m is the particle mass, $\dot{\mathbf{u}}_r$ is the acceleration of particle r , \mathbf{f}_r is the fluid-particle interaction force exerted on particle r by the fluid (and includes the lubrication, drag and buoyancy forces), while \mathbf{f}_{rs}^c and \mathbf{f}_{rs}^i are the forces exerted by particle s on particle r due to the direct contact and the repulsion between the particles, respectively (for a given particle r , these forces are nonzero only for a small subset of particles s). Eq. 8

is the balance equation for the angular momentum, where I is the moment of inertia of the particles about their centers, $\dot{\omega}_r$ is the angular acceleration of particle r , while \mathbf{l}_r , \mathbf{l}_{rs}^c and \mathbf{l}_{rs}^\bullet are the torques acting on particle r generated by the fluid-particle interaction force exerted by the fluid on particle r and by the direct contact forces and lubrication forces between particles r and s , respectively.

III. CLOSURE EQUATIONS

In this section, we report the closure equations adopted to close the model presented in the previous section. Then, we present the equations of the Eulerian-Eulerian and mixture models, which are used to define and calculate the suspension stress tensor and in turn the suspension viscosity.

A. Fluid-particle interaction force

The fluid-particle interaction force $n\langle \mathbf{f} \rangle_p$ in Eq. 2 arises from the gradients of the point velocity of the ambient fluid generated over the surface of the particles. Similarly to the particle-presence stress, this force is related to the distortion of the fluid streamlines caused by the particles and to the lubrication films between particle pairs. Therefore, we split the force in two parts:

$$n\langle \mathbf{f} \rangle_p = n\langle \mathbf{f} \rangle_p^* + n\langle \mathbf{f} \rangle_p^\bullet \quad (9)$$

The first term on the right-hand side is related to the distortion of the fluid streamlines around the particles, while the second term is the contribution of the lubrication films. $n\langle \mathbf{f} \rangle_p^*$ can be expressed as the divergence of the part of the particle-presence stress related to the lubrication films¹⁷:

$$n\langle \mathbf{f} \rangle_p^* = -\partial_{\mathbf{x}} \cdot n\langle \mathbf{A} \rangle_p^* \quad (10)$$

Several constitutive equations are available for $n\langle \mathbf{f} \rangle_p^*$. Here, we consider only the buoyancy and drag forces, writing:

$$n\langle \mathbf{f} \rangle_p^* = -\phi\partial_{\mathbf{x}} \cdot \langle \mathbf{S} \rangle_e^* + n\beta(\langle \mathbf{u} \rangle_e - \langle \mathbf{u} \rangle_p) \quad (11)$$

where ϕ denotes the volume fraction of the particles (or solid volume fraction) in the suspension. The first term on the right-hand side is the part of the buoyancy force related to the fluid effective stress tensor associated with the distortion of the fluid streamlines. The second term is the drag force, β being the drag force coefficient referred to one particle. Combining Eqs. 9 through 11, and then using Eq. 6, we obtain:

$$\begin{aligned} n\langle \mathbf{f} \rangle_p &= -\phi\partial_{\mathbf{x}} \cdot \langle \mathbf{S} \rangle_e \\ &+ n\beta(\langle \mathbf{u} \rangle_e - \langle \mathbf{u} \rangle_p) - \varepsilon\partial_{\mathbf{x}} \cdot n\langle \mathbf{A} \rangle_p^* \end{aligned} \quad (12)$$

The first term on the right-hand side represents the total buoyancy force, in line with the definition given by Jackson^[18].

The fluid-particle interaction force featuring in Eq. 7 reads:

$$\mathbf{f}_r = -V_p\partial_{\mathbf{x}} \cdot \langle \mathbf{S} \rangle_e^* + \mathbf{f}_{d,r} + \sum_s \mathbf{f}_{rs}^\bullet \quad (13)$$

where the first term on the right-hand side accounts for the buoyancy force associated with the distortion of the fluid streamlines. \mathbf{f}_{rs}^\bullet is the lubrication force, $\mathbf{f}_{d,r}$ is the drag force and V_p is the particle volume.

B. Lubrication force

As outlined in the introduction, we use the unresolved Eulerian-Lagrangian modeling approach. Thus, since the fluid dynamics is not resolved around the particles, we must model the lubrication forces between the particles. For this, we use the short-ranged, frame-invariant and pairwise force closure derived by Jeffrey and Onishi^[19] and Jeffrey^[20], and adapted by Cheal and Ness^[21] for DEM simulations. The lubrication force exerted on particle r by particle s takes the form:

$$\begin{aligned} \mathbf{f}_{rs}^\bullet &= \eta_e \{ [X_{11}^A \mathbf{k}_{rs} \mathbf{k}_{rs} + Y_{11}^A (\delta - \mathbf{k}_{rs} \mathbf{k}_{rs})] \cdot (\mathbf{u}_s - \mathbf{u}_r) \\ &- Y_{11}^B (\boldsymbol{\omega}_r \times \mathbf{k}_{rs}) - Y_{21}^B (\boldsymbol{\omega}_s \times \mathbf{k}_{rs}) \} \end{aligned} \quad (14)$$

where η_e is the viscosity of the Newtonian ambient fluid, \mathbf{k}_{rs} is the unit vector pointing from the center of particle r to the center of particle s , δ is the identity tensor, while \mathbf{u}_r and $\boldsymbol{\omega}_r$ are the linear and angular velocities of particle r , respectively. The torque is given by:

$$\begin{aligned} \mathbf{l}_{rs}^\bullet &= -\eta_e [Y_{11}^B (\mathbf{u}_s - \mathbf{u}_r) \times \mathbf{k}_{rs} \\ &+ (\delta - \mathbf{k}_{rs} \mathbf{k}_{rs}) \cdot (Y_{11}^C \boldsymbol{\omega}_r + Y_{12}^C \boldsymbol{\omega}_s)] \end{aligned} \quad (15)$$

For the expressions of the scalar resistances X_{11}^A , Y_{11}^A , Y_{11}^B , Y_{21}^B , Y_{11}^C , Y_{12}^C and Y_{12}^B , we refer to Cheal and Ness^[21]. The lubrication force modeled via Eq. 14 diverges at contact, but it is customary to set the force to zero for surface to surface particle distances smaller than approximately 0.1% of the particle radius. The part of the particle-presence stress tensor related to the lubrication forces, featuring in Eq. 6, is given by:

$$n\langle \mathbf{A} \rangle_p^\bullet \equiv \frac{a}{V_a} \sum_r \sum_s \mathbf{k}_{rs} \mathbf{f}_{rs}^\bullet \quad (16)$$

where a is the particle radius and the two sums are over all the particles r and s present in the averaging region. V_a is the volume of the region over which the local volume average is calculated. This region must be large enough to contain several particles, so that the average is statistically meaningful, but its characteristic size must be far smaller than the length scale characterizing the spatial variations of the mean fields, so that these variations are correctly captured.

C. Drag force

The drag force featuring in Eq. 13, that is, the drag force exerted by the fluid on particle r , is taken to be proportional to the difference between the mean velocity of the fluid and the velocity of particle r . So, we have:

$$\mathbf{f}_{d,r} \equiv \beta(\langle \mathbf{u} \rangle_e - \mathbf{u}_r) \quad (17)$$

where β is the drag force coefficient and \mathbf{u}_r is the velocity of particle r . The volume averaged drag force for the fluid phase, featuring in Eq. 12, is given by:

$$n\langle \mathbf{f}_d \rangle_p \equiv \frac{1}{V_a} \sum_r \mathbf{f}_{d,r} \quad (18)$$

where the sum is over all particles r in the averaging volume. In the literature, there are various closures for β . Here, we use that by Di Felice^[22], written consistently with the definition of buoyancy force used in Eq. 11:

$$\begin{aligned} \beta &= \left[(\pi a^2) \frac{1}{2} \rho_e |\langle \mathbf{u} \rangle_e - \langle \mathbf{u} \rangle_p| C_D(\text{Re}) \right] \varepsilon^{2-\alpha} ; \\ \alpha &= 3.7 - 0.65 \exp \left[\frac{-(1.5 - \log_{10} \text{Re})^2}{2} \right] \end{aligned} \quad (19)$$

where the mean velocity of the solid phase is defined as:

$$n\langle \mathbf{u} \rangle_p \equiv \frac{1}{V_a} \sum_r \mathbf{u}_r \quad (20)$$

and the Reynolds number Re and the friction coefficient C_D are given by:

$$\text{Re} \equiv \frac{\varepsilon \rho_e |\langle \mathbf{u} \rangle_e - \langle \mathbf{u} \rangle_p| 2a}{\eta_e} \quad (21)$$

$$C_D = \left(0.63 + \frac{4.8}{\sqrt{\text{Re}}} \right)^2 \quad (22)$$

Eq. 19 features the mean velocity of the solid phase, so β has the same value for all the particles contained in the averaging volume. This ensures that Eq. 18 yields the correct expression of the mean drag force per unit volume of suspension:

$$n\langle \mathbf{f}_d \rangle_p = n\beta(\langle \mathbf{u} \rangle_e - \langle \mathbf{u} \rangle_p) \quad (23)$$

In Eq. 8, for the term \mathbf{l}_r , we account only for the rotational component of the drag force. At low Reynolds numbers, this is often modeled by the Stokes torque:

$$\mathbf{l}_r = 8\pi\eta_e a^3 (\langle \boldsymbol{\omega} \rangle_e - \boldsymbol{\omega}_r) \quad (24)$$

where $\langle \boldsymbol{\omega} \rangle_e$ is the mean angular velocity of the fluid, given by the axial vector associated with the antisymmetric part of the gradient of the fluid mean velocity field. Many studies, such as those by Blais and Bertrand^[4] and Liu *et al.*^[23], disregard the Stokes torque. As shown by Bnà *et al.*^[24], its influence is negligible for particles with diameters up to several tens of microns. In light of this, and after verifying that this term is indeed negligible for the systems herein considered, we have omitted it in our simulations.

D. Contact force

To model the contact forces between the particles, we adopt the spring-dashpot model^[25]. In it, the (absolute) normal and

tangential particle overlaps, δ^n and δ^t , respectively, together with the relative particle collision velocities in the normal and tangential directions, u_{rs}^n and u_{rs}^t , respectively, are employed to calculate the normal and tangential parts of \mathbf{f}_{rs}^c as well as the torque \mathbf{l}_{rs}^c . These are modeled as follows:

$$\mathbf{f}_{rs}^c = \mathbf{f}_{rs}^{c,n} + \mathbf{f}_{rs}^{c,t} \quad (25)$$

$$\mathbf{f}_{rs}^{c,n} = -(k^n \delta^n + \eta^n u_{rs}^n) \mathbf{k}_{rs} \quad (26)$$

$$\mathbf{f}_{rs}^{c,t} = -(k^t \delta^t + \eta^t u_{rs}^t) \mathbf{t}_{rs} \quad (27)$$

$$\mathbf{l}_{rs}^c = a \mathbf{k}_{rs} \times \mathbf{f}_{rs}^{c,t} \quad (28)$$

with:

$$\mathbf{u}_{rs} \equiv \mathbf{u}_r - \mathbf{u}_s + a(\boldsymbol{\omega}_r + \boldsymbol{\omega}_s) \times \mathbf{k}_{rs} \quad (29)$$

$$u_{rs}^n \equiv \mathbf{u}_{rs} \cdot \mathbf{k}_{rs} ; \quad u_{rs}^t \equiv \mathbf{u}_{rs} \cdot \mathbf{t}_{rs} \quad (30)$$

where $\delta^t \mathbf{t}_{rs}$ denotes the incremental tangential displacement, reset at the initiation of each contact, while k and η are the spring and damping coefficients, respectively. The tangential force is truncated to fulfill Coulomb's law of friction $|\mathbf{f}_{rs}^{c,t}| \leq \mu |\mathbf{f}_{rs}^{c,n}|$, with μ denoting the friction coefficient. The tangential dashpot has no physical significance and is primarily used in granular media simulations as an efficient numerical stabilizer. Following Mari *et al.*^[15], we set the tangential damping to zero. The absolute value of the spring coefficient does not affect the magnitude of the collision forces, unless the particles are “too soft”, the particles overlap exceeding $\sim 4\%$ of their radius²⁶. The normal spring coefficient is calculated from the material properties²⁷:

$$k^n = \frac{16}{15\sqrt{2}} \sqrt{a} Y^* \left(\frac{15\sqrt{2} m v_{ch}^2}{32\sqrt{a} Y^*} \right)^{1/5} \quad (31)$$

while the normal damping coefficient is given by:

$$\eta^n = \frac{2mk^n}{1 + \left(\frac{\pi}{\ln e} \right)^2} \quad (32)$$

where v_{ch} is a parameter that should reflect the characteristic impact velocity between particle pairs, but whose value is often set to fine tune the normal spring coefficient, e is the restitution coefficient (equal to unity for elastic particle collisions) and Y^* is a material property defined as:

$$Y^* \equiv \frac{Y}{2(1 - \nu^2)} \quad (33)$$

where Y and ν are the Young modulus and the Poission ratio, respectively. The tangential spring coefficient is set equal to the normal one ($k^t = k^n$)¹⁵.

E. Repulsive force

We use a repulsive force similar to the electrostatic double layer force:

$$\mathbf{f}_{rs}^i = -F_0 e^{-(h - \delta_{rs})\kappa} \mathbf{k}_{rs} \quad (34)$$

where F_0 is the force at contact, h is the interparticle surface distance and κ^{-1} is the Debye length. δ_{rs} is the sum of the widths of the asperities for particles r and s ; for $h \leq \delta_{rs}$, the force \mathbf{f}_{rs}^i is set to be constant and equal to $-F_0 \mathbf{k}_{rs}$. The theoretical Debye length is given by²⁸:

$$\kappa^{-1} = \left[\frac{\varepsilon_e \varepsilon_0 \hbar T}{2q^2 E} \right]^{1/2} \quad (35)$$

where E is the ionic strength, q is the electric charge, ε_0 is the permittivity of vacuum, ε_e is the relative dielectric constant of the liquid, \hbar is the Planck constant and T is the absolute temperature. For typical values of E , Eq. 35 yields a Debye length between 1 and 10 nm, but in the literature far greater values have been considered (Mewis and Wagner^[29], Châté *et al.*^[30] and Mari *et al.*^[15]); here, we make the Debye length range between 0.0005 a (order of magnitude given by Eq. 35) and 0.05 a (order of magnitude of the cited articles).

F. Particle-presence stress

Consider $\langle \mathbf{S} \rangle_e^*$ in Eq. 5. The first term on the right-hand side is the averaged fluid point stress tensor; this can be closed with the expression reported by Joseph *et al.*^[31]:

$$\varepsilon \langle \boldsymbol{\sigma} \rangle_e = \varepsilon \langle p \rangle_e \boldsymbol{\delta} - \eta_e \langle \dot{\gamma} \rangle_e \quad (36)$$

where $\langle p \rangle_e$ is the fluid mean pressure and $\langle \dot{\gamma} \rangle_e$ is twice the deformation rate tensor for the fluid. This expression is valid if the mean velocity of the solid is (approximately) equal to that of the fluid¹⁷. A closure for $n \langle \mathbf{A} \rangle_e^*$ has been derived for dilute systems; for suspensions with a solid volume fraction up to 5%, the equation derived by Jackson^[3] holds:

$$n \langle \mathbf{A} \rangle_e^* = \phi \langle p \rangle_e \boldsymbol{\delta} - \eta_e (5/2) \phi \langle \dot{\gamma} \rangle_e \quad (37)$$

The last term on the right-hand side of Eq. 5 is a Reynolds stress type of contribution and for the flow investigated is negligible¹⁶. Summing the first two contributions gives:

$$\langle \mathbf{S} \rangle_e^* = \varepsilon \langle \boldsymbol{\sigma} \rangle_e + n \langle \mathbf{A} \rangle_e^* = \langle p \rangle_e \boldsymbol{\delta} - \eta_m \langle \dot{\gamma} \rangle_e \quad (38)$$

where η_m is the mixture viscosity with the Einstein correction:

$$\eta_m = \eta_e [1 + (5/2)\phi] \quad (39)$$

Eq. 38 has been extended to higher solid volume fractions, with η_m given by³²:

$$\eta_m = \eta_e (1 + D\phi + F\phi^2) \quad (40)$$

In this work, we use the coefficients derived by Batchelor and Green^[33], where D is the Einstein coefficient (taken as 2.5) and F is 7.6 (the value that applies to non-Brownian suspensions). Note that Eq. 40 has been reported to predict the *mixture viscosity* up to a solid volume fraction of approximately 20%³⁴. For larger solid volume fractions this does not suffice and other viscosity contributions, in particular that related to the lubrication forces, must be accounted for. This is done by considering the term $n \langle \mathbf{A} \rangle_p^*$, that is, the second term on the right-hand side of Eq. 6, which represents the part of the particle-presence stress associated with the lubrication forces. In our model, this term requires no closure, because it can be calculated via Eq. 16.

G. Suspension properties

As discussed, to simulate the dynamics of the solid phase, we employ the Lagrangian approach, tracking the motion of each single particle. These simulations do not directly provide information about the rheology of the suspension, and in particular do not yield the effective stress tensor of the solid phase; however, they do provide all the information that is needed to derive this quantity via averaging. The averaging process yields the solid stress tensor^{3;35}:

$$\langle \mathbf{S} \rangle_p \equiv n \langle \mathbf{B} \rangle_p^c + n \langle \mathbf{B} \rangle_p^i + \phi \rho_p \langle \hat{\mathbf{u}} \hat{\mathbf{u}} \rangle_p \quad (41)$$

where ρ_p is the density of the particles. The last term on the right-hand side of Eq. 41 is the kinetic stress tensor, which is related to the particle velocity fluctuations, and is negligible for the flow investigated¹⁶. $n \langle \mathbf{B} \rangle_p^c$ and $n \langle \mathbf{B} \rangle_p^i$ are the parts of the stress arising from direct particle contacts and interparticle (repulsive) forces, respectively:

$$n \langle \mathbf{B} \rangle_p^c \equiv \frac{a}{V_a} \sum_r \sum_s \mathbf{k}_{rs} \mathbf{f}_{rs}^c \quad (42)$$

$$n \langle \mathbf{B} \rangle_p^i \equiv \frac{a}{V_a} \sum_r \sum_s \mathbf{k}_{rs} \mathbf{f}_{rs}^i \quad (43)$$

where \mathbf{f}_{rs}^c is the force arising from direct particle contacts and \mathbf{f}_{rs}^i is the interparticle (repulsive) force. The stress tensor for the suspension is given by⁵:

$$\langle \mathbf{S} \rangle_m \equiv \langle \mathbf{S} \rangle_e + \langle \mathbf{S} \rangle_p + \langle \mathbf{S} \rangle_d \quad (44)$$

where the last term denotes the diffusion stress tensor:

$$\langle \mathbf{S} \rangle_d \equiv \varepsilon \phi \rho_e \rho_p (\langle \mathbf{u} \rangle_p - \langle \mathbf{u} \rangle_e) (\langle \mathbf{u} \rangle_p - \langle \mathbf{u} \rangle_e) \quad (45)$$

We assume that the Stokes number related to the mean velocity fields of the fluid and solid phases is much smaller than unity. In this case, the slip velocity between the phases is small and the diffusion stress tensor can be neglected.

To calculate the viscosity of the suspension, we employ the generalized Newtonian constitutive equation for $\langle \mathbf{S} \rangle_m$. Thus, we can define the viscosity as follows:

$$\mu_m \equiv \left| \frac{\langle \boldsymbol{\tau} \rangle_m : \langle \dot{\gamma} \rangle_m}{\langle \dot{\gamma} \rangle_m : \langle \dot{\gamma} \rangle_m} \right| \quad (46)$$

where $\langle \boldsymbol{\tau} \rangle_m$ is the deviatoric part of $\langle \mathbf{S} \rangle_m$ and $\langle \dot{\gamma} \rangle_m$ is twice the deformation rate tensor of the mixture velocity field. In the assumption that the particles are neutrally buoyant and the Stokes number is small, the mean velocity fields of the fluid, of the solid and of the mixture are (nearly) all identical. $\langle \boldsymbol{\tau} \rangle_m$ and $\langle \dot{\gamma} \rangle_m$ are locally averaged properties; thus, Eq. 46 yields a viscosity field, that is, the value of the suspension viscosity in every spatial point occupied by the suspension. Since the suspension is non-Newtonian, we expect μ_m to be a function of the shear rate. For general flows, this is defined as:

$$|\langle \dot{\gamma} \rangle_m| \equiv [(1/2) \langle \dot{\gamma} \rangle_m : \langle \dot{\gamma} \rangle_m]^{1/2} \quad (47)$$

To calculate the mixture viscosity (Eq. 46), we must define the deviatoric part of the suspension stress tensor:

$$\begin{aligned}\langle \boldsymbol{\tau} \rangle_m &\equiv \langle \boldsymbol{\tau} \rangle_e + \langle \boldsymbol{\tau} \rangle_s \\ &= \eta_m \langle \dot{\gamma} \rangle_e + n \langle \mathbf{C} \rangle_p^{\bullet} + n \langle \mathbf{D} \rangle_p^c + n \langle \mathbf{D} \rangle_p^i\end{aligned}\quad (48)$$

where $n \langle \mathbf{C} \rangle_p^{\bullet}$, $n \langle \mathbf{D} \rangle_p^c$ and $n \langle \mathbf{D} \rangle_p^i$ are the deviatoric parts of the lubrication (Eq. 16), contact (Eq. 42) and interparticle (Eq. 43) stress tensors, respectively. We refer to the stress components on the right-hand side of Eq. 48 as “B-G” (Batchelor-Green), “Lubrication”, “Contact” and “Repulsive” stress, respectively. Note that $\langle \dot{\gamma} \rangle_e$ (and $\langle \dot{\gamma} \rangle_m$) is traceless. To prove this, let us consider a generic flow where the Stokes number is small, so that the slip velocity between the fluid and solid phases is also small and can be approximated to be zero, so that both phases move at the same velocity. Assuming that the fluid and solid phases are incompressible, the continuity equations read:

$$\partial_t \varepsilon = - \partial_{\mathbf{x}} \cdot (\varepsilon \langle \mathbf{u} \rangle_e) \quad ; \quad \partial_t \phi = - \partial_{\mathbf{x}} \cdot (\phi \langle \mathbf{u} \rangle_p) \quad (49)$$

Summing these two equations gives:

$$\partial_t (\varepsilon + \phi) = - \partial_{\mathbf{x}} \cdot (\varepsilon \langle \mathbf{u} \rangle_e + \phi \langle \mathbf{u} \rangle_p) \quad (50)$$

But $\varepsilon + \phi = 1$, so the time derivative on the left-hand side vanishes. On the right-hand side, taking $\langle \mathbf{u} \rangle_e = \langle \mathbf{u} \rangle_p$, we get $\partial_{\mathbf{x}} \cdot \langle \mathbf{u} \rangle_e = 0$. Now, the trace of the rate of deformation tensor associated with $\langle \mathbf{u} \rangle_e$ is equal to $\partial_{\mathbf{x}} \cdot \langle \mathbf{u} \rangle_e$. Therefore, from the last equation above, we conclude that, for any flow, this tensor is traceless.

IV. SIMULATION CAMPAIGN

We set up the simulations for a 3D simple shear flow with periodic boundaries in all directions except that normal to the shearing plane. In the normal direction, at the bottom and top of the domain, there are two horizontal solid plates, one motionless and one moving horizontally at a velocity equal to $\dot{\gamma} L_z$, where $\dot{\gamma}$ is the nominal shear rate characterizing the flow and L_z is the distance between the plates, see Fig. 1. L_z is chosen to be two orders of magnitude larger than the particles to ensure separation of scales. In the two periodic sides, the separation of scales condition is not as strict, so we set L_x^p and L_y^p equal to $\sim 50a$. Key particle properties include the particle radius a , density ρ_p , normal stiffness k^n , and friction coefficient μ . In the simulations, the fluid phase and particle phase are simulated separately with their own time steps and at a given interval they are coupled and exchange forces⁴. Both the fluid and particle time steps are critical for a stable and accurate simulation. There is a regime of particle time steps where the simulation is stable but generates unphysically large relative particle velocities. To address this issue, we derived a new time step criterion specifically for overdamped systems, accounting for the lubrication forces (see Appendix A). To ensure physically realistic simulations, the following quantities

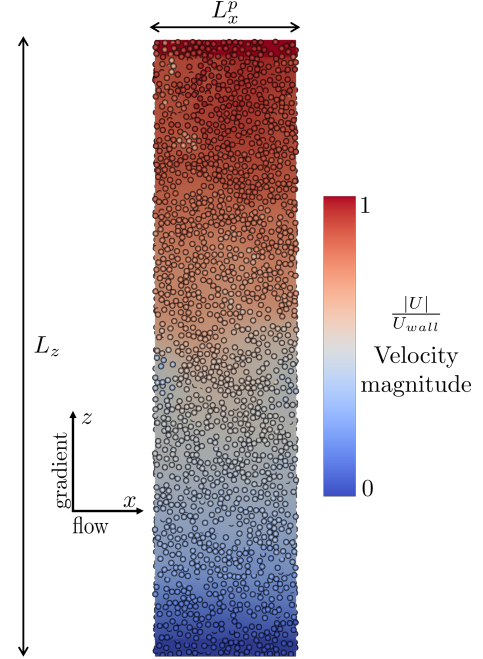


FIG. 1: Example of simulation setup showing a snapshot under steady-state conditions of the fluid and particle velocity fields. The particles are non-repulsive and the solid volume fraction is 50%. The particles are shown with equal size colored according to the velocity magnitude scale. The background color is the fluid velocity field.

must be significantly smaller than unity:

- (i) a/L_z
- (ii) $\rho_p \dot{\gamma} a^2 / \eta_e$
- (iii) $6\pi\eta_e a \dot{\gamma} / k^n$
- (iv) $\frac{(3/2)\pi a^2 \eta_e / \delta - \sqrt{((3/2)\pi a^2 \eta_e / \delta)^2 - 4mk^n}}{\Delta t_D k^n}$

Condition (i) ensures bulk conditions, condition (ii) ensures no particle inertia and condition (iii) ensures rigid particles. Condition (iv) ensures a physical and stable simulation, where Δt_D is the DEM time step, $\delta/2$ is the width of the particle asperities and m is the mass of a particle. Additionally, we introduced bidispersity to prevent the formation of ordered phases observed in dense suspensions consisting of particles of the same size under shear. We chose a size ratio of $a_2/a_1 = 1.4^{36}$, the two particle classes having the same volume fraction.

These conditions ensure that under constant friction (μ) and steady-state conditions, the viscosity is only a function of the volume fraction. Adding repulsive interparticle forces to the system is thus the only force scale that can introduce a shear rate dependence for the mixture viscosity.

The equations from previous sections are implemented in the open-source “CFDEM” software, an extension of the CFD software OpenFOAM and the DEM software LIGGGHTS. The model parameters are summarized in Table I.

Fig. 1 shows a snapshot of the simulation, with L_z representing the vertical length in the direction of the velocity gradient and L_x^p the (periodical) horizontal length in the direc-

TABLE I: Parameters used in the simulations. x denotes the direction parallel to the flow, z denotes the direction normal to the shearing plane and y denotes the direction normal to x and z . The flow is periodic in the x and y directions.

Quantity	Symbol	Unit	Value
System geometry	$L_x^p \times L_y^p \times L_z$	mm	$0.23 \times 0.23 \times 1$
CFD cells	$N_x \times N_y \times N_z$	-	$7 \times 7 \times 33$
Fluid viscosity	η_e	Pa·s	$1 \cdot 10^{-3}$
Fluid density	ρ_e	kg/m ³	$1 \cdot 10^3$
Type 1 - radius	a_1	μm	5
Type 2 - radius	a_2	μm	7
Particle density	ρ_p	kg/m ³	$1 \cdot 10^3$
Type 1 - asperity width	$\delta_1/2$	nm	5
Type 2 - asperity width	$\delta_2/2$	nm	7
Top wall velocity (x)	U_{wall}	m/s	0.5
Debye length	κ^{-1}	nm	250, 125, 25, 2.5
Friction coefficient	μ	-	1
Young's modulus	Y	Pa	$3 \cdot 10^8$
Poisson ratio	ν	-	0.3
Restitution coefficient	e	-	0.9
Characteristic velocity	v_{ch}	m/s	100
CFD time step	Δt_C	s	10^{-7}
DEM time step	Δt_D	s	10^{-8}
Boundary conditions	-	-	No slip / Periodic

tion of the flow. A velocity difference between the horizontal walls, U_{wall} , imposes a nominal shear rate of $\dot{\gamma} = U_{wall}/L_z$.

V. A SIMPLE PHYSICAL MODEL

In this section, we introduce a minimal physical model that encapsulates the fundamental physical characteristics of the investigated system. This model will serve as a valuable tool for interpreting the simulation results.

A. Newtonian rheology

Consider a particle pair in a suspension undergoing a shearing flow in the absence of repulsive interparticle forces. Particle 1 is fixed relative to the coordinate system, while particle 2 approaches with a velocity on the order of magnitude of $\dot{\gamma}a$. In the Stokesian limit, the inertia of the particle is negligible, so the drag force always balances the lubrication force. Thus, we can write:

$$6\pi\eta_e a(\dot{\gamma}a - v)\varepsilon^{-3.70} = (3/2)\pi a^2 \eta_e (v/h) \quad (51)$$

where the right-hand side describes the order of magnitude of the lubrication force (Eq. 14). h is the interparticle surface distance and v is the relative particle velocity. Note the inclusion of the *hindrance function*, $\varepsilon^{-3.70}$, which previous works have omitted. Although we focus on two particles, these are

part of a suspension, and the drag force acting on particle 2 is influenced by the surrounding particles. The justification of its inclusion is detailed in Appendix B.

Owing to the lubrication force, as the particles approach, particle 2 decelerates, so the relative particle velocity v reduces. Consequently, the slip velocity between the fluid and particle 2, and hence the drag force acting on particle 2, increases, pushing the particles closer together. Assuming that the lubrication film breaks down at a given cut-off length, the particles will always collide in a finite time. Moreover, since in the case we are considering (rigid, non-Brownian particles in the Stokes regime and in the absence of interparticle forces) the only force scale present in the system is the fluid dynamic one, the rheology of the suspension is Newtonian, regardless of whether the particles are frictionless or frictional.

For a given $\dot{\gamma}$, as the solid volume fraction increases, the viscosity of the suspension increases, diverging as ϕ approaches the jamming volume fraction ϕ_j . If the relative viscosity of the suspension (normalized by the ambient fluid viscosity η_e) follows the typical power law, then:

$$\eta_r = C(1 - \phi/\phi_j)^{-\lambda} \quad (52)$$

This is the Krieger-Dougherty equation⁸, relating the viscosity of dense suspensions to solid volume fraction and jamming volume fraction. In general, C and λ are taken as empirical constants; to retrieve the viscosity correction of Einstein^[37], C and λ must be set to 1 and 2.5, respectively. The Kepler conjecture states that the maximum volume fraction of identical rigid spheres is equal to $\pi/(3\sqrt{2}) \approx 0.74$. This value is only attained when the particles are arranged in a regular crystalline structure. De Laat, De Oliveira Filho, and Valletin^[38] found the upper bound volume fraction for particles of a radii ratio of 1:1.4 to be approximately 0.8; this value was obtained via a numerical approach for packing of spheres of different radii assuming a regular crystal arrangement. Such large packing fractions require particles to slip past each other unhindered and is never reached in practice. Instead, suspensions jam at a considerably lower volume fraction because the particles create a network of contacts with associated forces. At a microscopic level, the strength of a particle network does not solely originate from particle-to-particle friction but also stems from the entanglement of particles resisting the flow. Hence, even frictionless particles (for which the particle friction coefficient μ is zero) form networks of particle contacts and exhibit a nonzero macroscopic friction coefficient³⁹. A network of frictionless particles (where the contact forces between the particles are normal to the particle surfaces) cannot resist the flow to the same degree as a network of frictional particles (where the contact forces between the particles include components that are both normal and tangential to the particle surfaces). Thus, a network of frictionless particles is weaker than a network of frictional particles and can accommodate a larger solid volume fraction before it jams. Hence, frictionless suspensions generally have a jamming volume fraction of $\phi_j \approx 0.64$, while frictional suspensions jam at a solid volume fraction of $\phi_j \approx 0.57$.⁶

B. Shear-thickening rheology

To get a shear-thickening behavior, we must introduce a force scale⁴⁰. Assume a repulsive force acts between the particles, the force being zero when the particle distance exceeds a length κ^{-1} , representing the force range, with maximum magnitude F_0 when the particles touch at $h = \delta$. Thus, F_0 serves as the repulsive force scale. On the other hand, the drag force scale is $6\pi\eta_e a^2 \dot{\gamma} \varepsilon^{-3.70}$. Thus, to judge whether the repulsive force is negligible or not, we must consider the dimensionless number given by the ratio of these two force scales; alternatively, we can compare the value of the shear rate to the following characteristic shear rate value:

$$\dot{\gamma}^* \equiv \frac{F_0}{6\pi\eta_e a^2 \varepsilon^{-3.70}} \quad (53)$$

For $\dot{\gamma}/\dot{\gamma}^* \gg 1$, the drag force dominates, and particle interactions are well approximated by Eq. 51. Thus, the viscosity follows Eq. 52 with a jamming volume fraction ϕ_j of frictional particles. For $\dot{\gamma}/\dot{\gamma}^* \ll 1$, the repulsive force is significant and prevents particle contacts. Consequently, the particles behave as if they were frictionless. This results in a significant reduction in the solid stress, and in the suspension viscosity modeled by Eq. 52, ϕ_j takes on the value for frictionless particles. The gradual transition from frictionless to frictional contacts as $\dot{\gamma}/\dot{\gamma}^*$ exceeds unity results in a shear-thickening rheology. This transition is reflected by a change in the value of ϕ_j , which is larger for $\dot{\gamma}/\dot{\gamma}^* \leq 1$, where the particle network is weaker owing to the repulsive forces, and is smaller for $\dot{\gamma}/\dot{\gamma}^* > 1$, where the particle network is stronger owing to the frictional forces.

In the seminal work of Mari *et al.*^[15], the authors studied shear-thickening in suspensions, plotting their viscosity curves against a dimensionless shear rate in which the shear

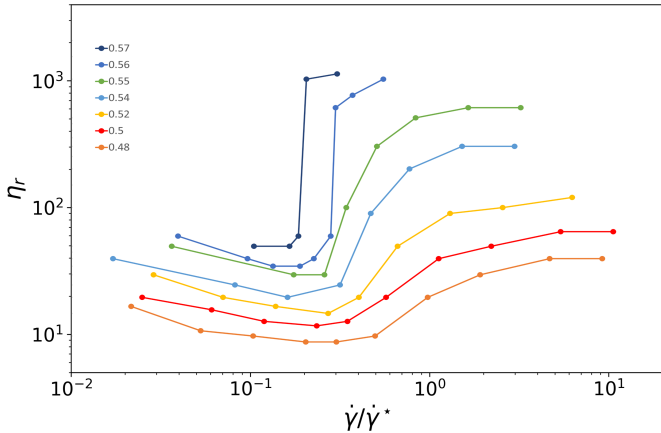


FIG. 2: Figure generated using the data reported in Fig. 4 of Mari *et al.*^[15]. The figure reports the relative viscosity η_r as a function of the dimensionless shear rate $\dot{\gamma}/\dot{\gamma}^*$ for repulsive particles with $\kappa^{-1} = 0.05a$ and solid volume fractions according to the legend. The characteristic shear rate $\dot{\gamma}^*$ has been redefined according to Eq. 53.

rate scale did not account for the hindrance function (see Eq. 53). If we study Fig. 4 of the article of Mari *et al.*, which reports the relative viscosity as a function of the dimensionless shear rate with $\dot{\gamma}^* \equiv F_0/6\pi\eta_e a^2$, we find that the shear-thickening starts in the range $\dot{\gamma}/\dot{\gamma}^* \sim 0.01 - 0.03$. In dense suspensions, the hindrance function cannot be neglected because it changes the magnitude of the drag force. For instance, in a suspension with a solid volume fraction of $\phi = 0.5$, the hindrance function takes a value of $\varepsilon^{-3.70} = 13$. In Fig. 2, we have adjusted the simulation data of Mari *et al.*^[15] by redefining the characteristic shear rate according to Eq. 53. In the revised figure, the curves shift and in all of them shear-thickening arises in the range where $\dot{\gamma}/\dot{\gamma}^*$ has unit order of magnitude, as one would expect. This reveals the importance of accounting for the hindrance function.

C. Shear-thinning rheology

In the Stokesian limit, the drag force must balance the lubrication force and the repulsive force (Eq. 34); thus, we have:

$$6\pi\eta_e a(\dot{\gamma}a - v)\varepsilon^{-3.70} = (3/2)\pi a^2 \eta_e (v/h) + F_0 e^{-(h-\delta)\kappa} \quad (54)$$

Setting $v = 0$, we obtain:

$$6\pi\eta_e a^2 \dot{\gamma} \varepsilon^{-3.70} = F_0 e^{-(h-\delta)\kappa} \quad (55)$$

whence:

$$(H - \delta)\kappa = \ln\left(\frac{\dot{\gamma}^*}{\dot{\gamma}}\right) \quad (56)$$

where H is the distance at which the repulsive force balances the largest value of the drag force. In these conditions, the suspension behaves as if it were formed by larger frictionless particles, referred to as *apparent particles*, with a radius equal to the radius of the actual particles (hard core) plus the thickness of a *soft shell* of liquid equal to half the equilibrium distance H . In other words, for $\dot{\gamma}/\dot{\gamma}^* \leq 1$, particle 2 stops at a distance H (from particle 1) greater than δ , so the system behaves as a suspension of larger contactless particles with radius $r \equiv a + H/2$. The corresponding jamming volume fraction of the actual particles, denoted as ϕ_j^* , is equal to:

$$\phi_j^* = \phi_j \left(\frac{r}{a}\right)^{-3} = \phi_j \left[1 + \frac{H}{2a}\right]^{-3} \quad (57)$$

where ϕ_j denotes the jamming volume fraction of the apparent (frictionless) particles, which will be referred to as *apparent jamming volume fraction*. Then, the viscosity of the suspension is:

$$\eta_r = C \left[1 - (\phi/\phi_j^*)\right]^{-\lambda} \quad (58)$$

As the ratio $\dot{\gamma}/\dot{\gamma}^*$ increases, H decreases (Eq. 56), ϕ_j^* increases (Eq. 57), and so the (relative) viscosity of the suspension decreases (Eq. 58). Hence, the suspension viscosity shear-thins, the shear-thinning behavior ending when the ratio $\dot{\gamma}/\dot{\gamma}^*$ reaches unity. Moreover, according to this model, when $\dot{\gamma}/\dot{\gamma}^*$ decreases sufficiently so that $\phi_j^* = \phi$, the suspension viscosity diverges and the suspension jams.

D. The apparent jamming volume fraction

The apparent jamming volume fraction ϕ_j can be regarded as the jamming volume fraction of a suspension of larger, frictionless, soft particles with a radius equal to $a + (H/2)$. Each apparent particle consists of a rigid core, represented by a real particle, and a liquid shell of thickness equal to $H/2$, with H given by Eq. 56. The apparent particles have soft interpenetrable shells and therefore are not equivalent to real frictionless rigid particles and should not be expected to behave exactly like them. Moreover, the equation for the added radius of the apparent particles is based on a simplified reasoning about a single particle pair. In reality, the particle pair is affected by the neighboring particles, and this effect cannot be fully accounted for merely via the hindrance function. Thus, also for this reason, the value of the apparent jamming volume fraction featuring in Eq. 57 should not be expected to coincide with the value of the jamming volume fraction of frictionless rigid particles.

VI. RESULTS AND DISCUSSION

This section presents the results from the model introduced in Sections II and III. In Section VI A, we present the viscosity as a function of the solid volume fraction for non-repulsive frictional and frictionless particles. This is done not only to validate our CFD-DEM model, but also to determine the values of the jamming volume fraction for these two systems and their relation to the microstructure of the suspensions (or equivalently to their particle networks). Section VI B discusses the simulation results for a suspension with $\phi = 0.55$ and $\kappa^{-1} = 0.05a$, and Section VI C examines the influence of the Debye length on the suspension rheology, extending the analysis to suspensions with $\kappa^{-1} = 0.025a$, $\kappa^{-1} = 0.005a$ and $\kappa^{-1} = 0.0005a$.

Our analysis builds on the discussion outlined in Section V, particularly focusing on the jamming volume fraction as a function of the dimensionless shear rate. Thus, when employing the classic and modified Krieger-Dougherty equations (Eqs. 52 and 58), we do not regard the parameters C and λ as functions of the friction coefficient μ or of the dimensionless shear rate $\dot{\gamma}/\dot{\gamma}^*$. Rheological data are plotted against shear rates, non-dimensionalized by the characteristic shear rate defined in Eq. 53. Eq. 46 yields a viscosity field, thus we plot the viscosity averaged over the entire domain. Suspensions are simulated over 50 units of strain, with viscosity averaged over the last 30 units, and error bars represent the temporal standard deviation.

A. Frictional and frictionless regimes

In this section, we consider non-repulsive suspensions, determine the values of the jamming volume fraction and discuss their relation to the particle network. We anticipate that for repulsive particles the suspension viscosity should approach that of rigid non-repulsive frictional particles for $\dot{\gamma}/\dot{\gamma}^* > 1$ and

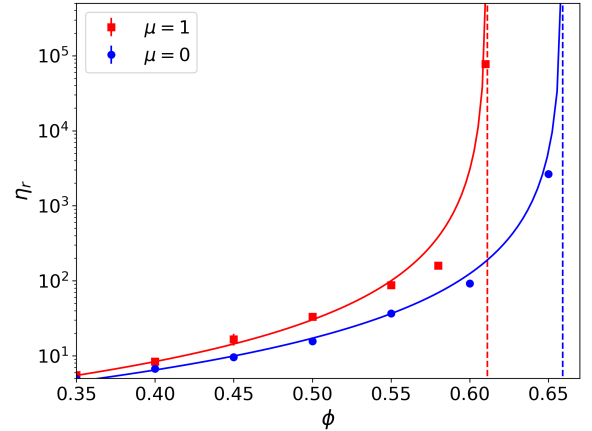


FIG. 3: Relative viscosity η_r as a function of the solid volume fraction ϕ . Red squares refer to frictional particles ($\mu = 1$) and blue dots to frictionless particles ($\mu = 0$). By fitting the red and blue curves with the Krieger-Dougherty equation (Eq. 52), we obtain $\phi_j = 0.66$, $\lambda = 2$, and $C = 1$ for the frictionless particles and $\phi_j = 0.61$, $\lambda = 2$, and $C = 1$ for the frictional particles. The dashed red and blue vertical lines mark the jamming volume fractions used during the fitting of Eq. 52 to the viscosity values of the frictional and frictionless particles, respectively.

that of rigid non-repulsive frictionless particles for $\dot{\gamma}/\dot{\gamma}^* \approx 1$. Fig. 3 reports the relative viscosity as a function of the volume fraction for non-repulsive particles with friction coefficients of $\mu = 1$ and $\mu = 0$. By fitting the Krieger-Dougherty equation (52) to the viscosity values obtained numerically, we retrieve the jamming volume fractions of the suspensions.

In Fig. 3, the red squares and the blue dots refer to the relative viscosities of the suspensions with a friction coefficient of $\mu = 1$ and $\mu = 0$, respectively. The red and blue solid curves are the plots of the Krieger-Dougherty equation (Eq. 52) with parameters $\phi_j = 0.61$, $\lambda = 2$, $C = 1$ and $\phi_j = 0.66$, $\lambda = 2$, $C = 1$, respectively. So, in what follows, we set $\lambda = 2$ and $C = 1$, considering ϕ_j as the only fitting parameter. The value of $\lambda \approx 2$ is consistent with experiments⁴¹ and simulations⁴² of spherical particle suspensions, although different values have also been reported (see, for instance, Zarraga, Hill, and Leighton^[43]).

The frictional suspension jams at a lower solid volume fraction than the frictionless suspension; thus, friction shifts the jamming point. Jamming occurs because the network of particles in contact spans the whole geometry and becomes sufficiently dense and strong as to hinder the flow of the suspension. In Fig. 4, we aim to visualize the link between the particle network and the jamming volume fraction. The figure visualizes a snapshot of a slice of the computational domain with a depth of two particle diameters, with all the particles in contact depicted with a red line connecting them. Both frictional and frictionless particles form networks spanning the whole geometry, but the frictional network is always denser. This confirms that a denser particle network translates into a lower value of the jamming volume fraction.

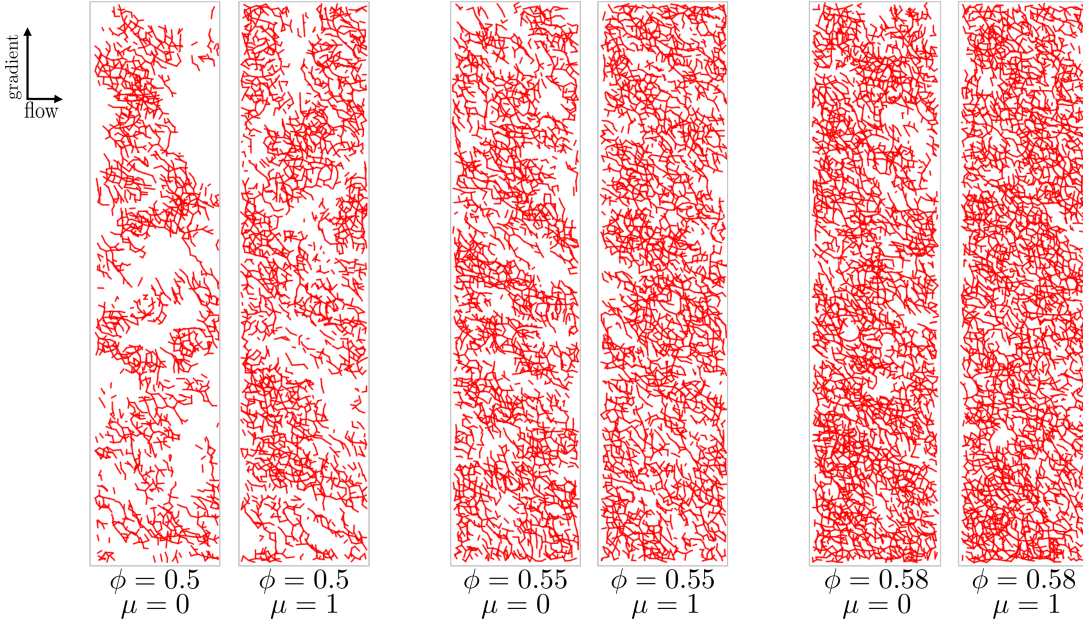


FIG. 4: 2D slice of the computational domain with a depth of two particle diameters. A red line identifies two particles in contact, connecting their centers. The particle networks are all connected and span the entire domain. A suspension with a lower jamming volume fraction has a denser particle network at the same solid volume fraction.

B. Analysis of the base case

In this section, we consider a repulsive suspension with a solid volume fraction of 0.55 and a Debye length of $0.05a$. This system is used as base case and is thus discussed in detail. To avoid repetition, we discuss the subsequent systems more succinctly. Fig. 5a reports our base case of a repulsive suspension with $\phi = 0.55$ and $\kappa^{-1} = 0.05a$. The horizontal dotted lines indicate the values of the relative viscosity for suspensions of frictional (blue) and frictionless (red) particles in the absence of repulsive forces. These values are taken from Fig. 3 with $\phi = 0.55$. The red squares represent the values of the relative viscosity for the suspension under investigation. Its various contributions (for instance, related to particle contacts, lubrication forces, and repulsive forces) are marked with colored lines and crosses according to the legend. “B-G” refers to the Batchelor-Green viscosity, whose value is very close to the theoretical value of 4.7 when $\phi = 0.55$ (see Eq. 40). The lubrication contribution, in orange, is significant but never dominates. “Contact”, in green, is the contribution related to the particle contact forces; at very small values of the dimensionless shear rate, since the particles are hindered from coming into contact, this contribution vanishes. When $\dot{\gamma}/\dot{\gamma}^*$ approaches unity, the equilibrium distance between the particles decreases, and the number of particles coming into contact gradually increases; consequently, the viscosity contribution due to particle contacts also gradually increases, eventually becoming the dominant quantity at large values of the dimensionless shear rate. At $\dot{\gamma}/\dot{\gamma}^* \gg 1$, the repulsive forces are insignificant and the value of the particle-contact viscosity essentially coincides with those of the suspension under investigation and of the corresponding suspension of rigid frictional

particles in the absence of repulsive forces (blue dotted line). The “Repulsive” viscosity contribution, in red, stems from the electrostatic double layer forces and is the leading viscosity component for small dimensionless shear rates. At $\dot{\gamma}/\dot{\gamma}^* \approx 1$, the rheology shifts from being dominated by repulsive forces to being dominated by contact forces, indicating that the non-dimensionlization of the shear rate (Eq. 53) is correct.

Fig. 5b reports the values of ϕ_j^* for the suspension under investigation. These values were obtained from the values of the suspension viscosity (plotted in Fig. 5a) and Eq. 58 (with $C = 1$ and $\lambda = 2$). In the shear-thinning region, as the dimensionless shear rate increases, the thickness of the fluid shells surrounding the particles (that is, H in Eq. 56) decreases, the jamming volume fraction accordingly increases, and the suspension finds itself further away from the jamming limit of non-repulsive, frictionless particles. So, as Eq. 57 indicates, ϕ_j^* is indeed expected to increase gradually. What may be less obvious is why, when the (order of magnitude of the) dimensionless shear rate exceeds unity, ϕ_j^* does not immediately jump to the value of the jamming volume fraction of rigid non-repulsive frictional particles. In this regard, we should note that the force balance equation reported in Section III serves as a simple guide to interpret the simulation results but does not capture the full complexity of particle interactions. It is not true that all the particles come into contact when the dimensionless shear rate exceeds unity; rather, the number of particles coming into contact is expected to increase gradually the more the dimensionless shear rate exceeds unity. As the number of direct contacts rises, so does the suspension viscosity. Consequently, according to Eq. 58, ϕ_j^* decreases gradually and eventually plateaus (in Fig. 5a, we see that the relative viscosity of the suspension behaves similarly). Note

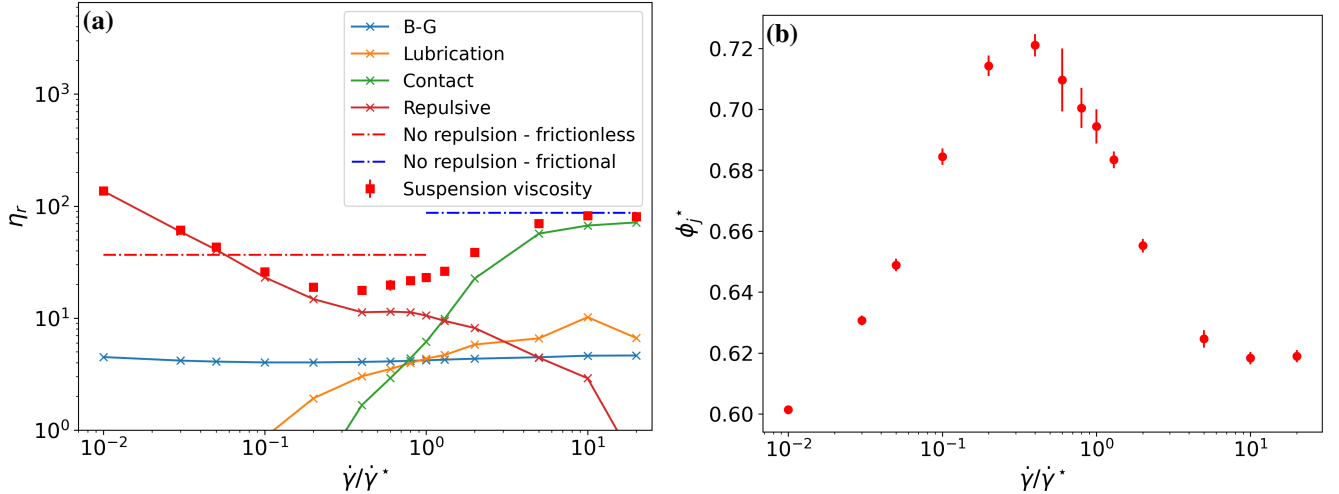


FIG. 5: (a) Relative viscosity η_r as a function of the dimensionless shear rate $\dot{\gamma}/\dot{\gamma}^*$ (red squares) for a suspension of repulsive particles with $\kappa^{-1} = 0.05a$ and $\phi = 0.55$. The various contributions to the suspension viscosity are also reported according to the legend. The horizontal dotted lines indicate the values of the relative viscosity for suspensions of frictional (blue) and frictionless (red) particles in the absence of repulsive forces. (b) Jamming volume fraction of the actual particles (Eq. 58) as a function of the dimensionless shear rate.

that the plateau value of $\phi_j^* \approx 0.62$ for large dimensionless shear rates is the same value reported in Fig. 3, represented by the red square point referring to $\phi = 0.55$ and $\mu = 1$; this value slightly differs from 0.61, which instead is the value obtained for $\phi = 0.55$ and $\mu = 1$ from the best-fit red line that fits all the red-square viscosity values reported in Fig. 3.

At $\dot{\gamma}/\dot{\gamma}^* \approx 1$, the fluid shells surrounding the particles are expected to be extremely thin; consequently, ϕ_j^* should not exceed 0.66, the value of the jamming volume fraction of the rigid frictionless particles (see Fig. 3). Contrary to this expectation, ϕ_j^* reaches a value of 0.72. To explain this behavior, let us first point out two important assumptions on which the arguments presented in Section III are based, which eventually result in Eq. 58. These assumptions are:

- The suspension can be regarded as consisting of apparent particles of radius $a + H/2$, with H given by Eq. 56. The value of H is calculated via a force balance that assumes that the apparent particles do not overlap.
- The relative viscosity of the suspension is well described by the Krieger-Dougherty equation written for the apparent particles. The microstructure of the suspension of apparent particles is similar to that of a suspension of rigid frictionless particles, so in Eq. 57, ϕ_j can be replaced by the jamming volume fraction of rigid frictionless particles.

Based on these assumptions, Eq. 58 ensues, with ϕ_j^* given by Eq. 57 and H given by Eq. 56. If all these assumptions were correct, one should not expect to observe the high values of ϕ_j^* reported in Fig. 5b. Since this expectation is not met, this seems to indicate that one or more of the assumptions reported above is incorrect. Therefore, we now examine them, considering them one at a time.

We start by testing the assumption concerning H . Does H estimate well the mean surface-to-surface distance between interacting apparent particles? Or do apparent particles partly overlap, so that the mean value of H is less than the theoretical value given by Eq. 56? To answer these questions, we determine the added radius by analyzing the histogram of the distribution of the surface-to-surface distances between particles interacting via repulsive forces. If H is a good estimate, we expect to find a peak in the histogram reflecting this. To measure the distance that corresponds to H , we cannot only consider the most common surface-to-surface distance, but we must also consider the repulsive force the particles are subjected to at their given distance; larger forces contribute more to the value of the viscosity, to which the value of H is ultimately related via Eqs. 56 and 58. A simple quantifiable measurement that takes these considerations into account is the force-weighted mean distance:

$$\bar{h} \equiv \frac{\sum h_{rs} |f_{rs}^i|}{\sum |f_{rs}^i|} \quad (59)$$

where h_{rs} is the surface-to-surface distance between particles r and s , while f_{rs}^i is the repulsive force between them, given by Eq. 34. In Fig. 6 we report the distribution histogram for the suspension with $\dot{\gamma}/\dot{\gamma}^* = 0.4$. This case is interesting because it represents the suspension with the largest value of the jamming volume fraction (see Fig. 5b). The weighted mean distance (\bar{h}), normalized by the equilibrium distance H , is marked by a red vertical line.

In Fig. 6, even though the distribution is broad, and a considerable number of particle cores are in direct contact (see $h/H = 0$), there is still a good match between the weighted mean distance (\bar{h}/H), the largest peaks of the histogram and the theoretical equilibrium distance ($h/H = 1$). This indicates that the theoretical value of H given by Eq. 56 appears to

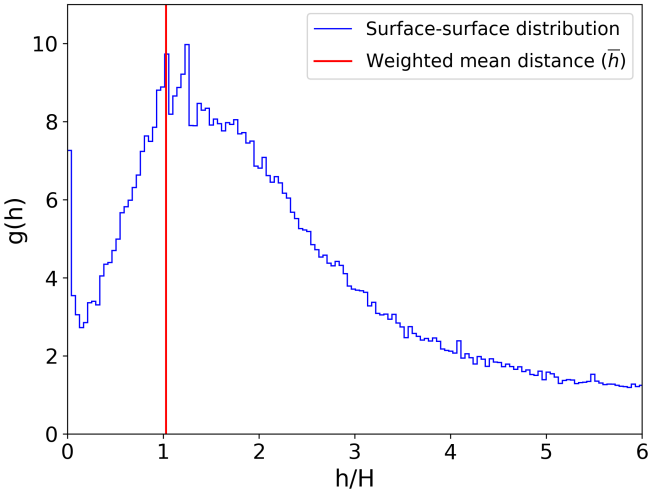


FIG. 6: Surface-to-surface distance distribution histogram (normalized with respect to the radial distribution of an ideal gas). The surface-to-surface particle distance (h) is normalized by the theoretical equilibrium distance (H , see Eq. 56). The normalized force-weighted mean distance (\bar{h}/H) of Eq. 59 is marked in red. $\dot{\gamma}/\dot{\gamma}^* = 0.4$, $\phi = 0.55$, $\kappa^{-1} = 0.05a$.

be a good estimate (the order of magnitude is correct); this in turn indicates that the unexpected behavior of ϕ_j^* is not caused by an inaccurate estimation of H . To test this further, in Fig. 7 we report \bar{h} and H as functions of the dimensionless shear rate for $\dot{\gamma}/\dot{\gamma}^* \leq 0.4$. As Fig. 7 shows, the theoretical equilibrium distance H slightly overestimates the weighted mean distance \bar{h} for $\dot{\gamma}/\dot{\gamma}^* < 0.4$ (the error being within 30%). But since the two quantities have the same order of magnitude, the slight overestimation of H cannot explain the unexpected high values of ϕ_j^* .

Next, we test the assumptions about the apparent jamming volume fraction (ϕ_j in Eq. 57). Since H estimates well the surface-to-surface particle distance, we employ Eq. 57 and the values of ϕ_j^* from Fig. 5b to obtain the corresponding values of ϕ_j . These values are reported in Fig. 8a.

The apparent jamming volume fraction reported in Fig. 8a behaves much like we expect. For low dimensionless shear rates, in the frictionless regime ($\dot{\gamma}/\dot{\gamma}^* \leq 0.4$), ϕ_j is relatively constant, indicating that the gradual decrease of ϕ_j^* in Fig. 5b is solely due to the gradual decrease in the added radius ($H/2$). As seen in Fig. 5a, in this regime the contact viscosity is insignificant and the apparent particle network consists only of frictionless contacts; thus, the contact forces associated with the network of apparent particles should be constant, and consequently also the apparent jamming volume fraction should be constant.

This is followed by a transitional regime where the dimensionless shear rate has unit order of magnitude, ($0.4 \leq \dot{\gamma}/\dot{\gamma}^* \leq 6$). As the number of particle cores in direct contact gradually increases, the suspension transitions from a network of frictionless contacts to a network of frictional contacts, and consequently also the apparent jamming volume fraction tran-

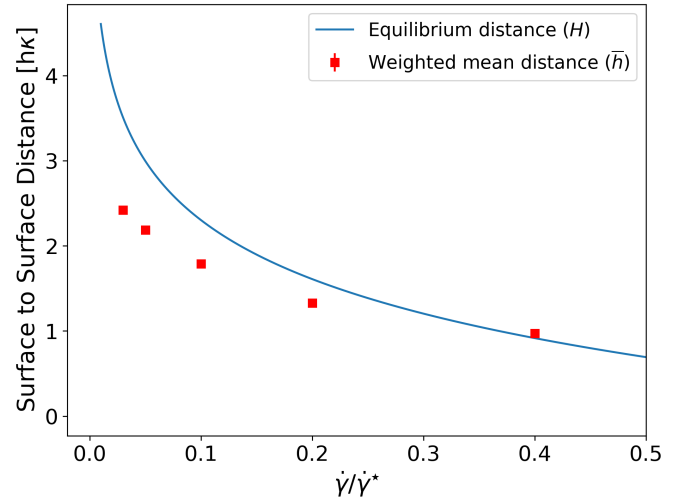


FIG. 7: Weighted mean distance (\bar{h}) and theoretical equilibrium distance (H) normalized by the Debye length (κ^{-1}) for a suspension with a solid volume fraction of $\phi = 0.55$, as a function of the dimensionless shear rate.

sitions from a value associated with frictionless contacts to a value associated with frictional contacts.

Finally, for large dimensionless shear rates, in the frictional regime ($\dot{\gamma}/\dot{\gamma}^* \geq 6$), frictional contacts dominate and the jamming volume fraction equals the jamming volume fraction of non-repulsive frictional particles.

In Fig. 8b, we report the relative viscosity marked in red squares and the modified Krieger-Dougherty equation (Eq. 58 with ϕ_j^* given by Eq. 57 with $\phi_j = 0.77$, $\lambda = 2$ and $C = 1$) using the apparent jamming volume fraction obtained from the frictionless regime in Fig. 8a, marked in green. The frictional viscosity from Fig. 3 is reported with the blue dotted line. As Fig. 8b shows, in the frictionless regime the modified Krieger-Dougherty equation (Eq. 58) matches the numerical results well; however, the apparent jamming volume fraction ($\phi_j \approx 0.77$) is considerably larger than that for frictionless particles ($\phi_j \approx 0.66$).

This result ($\phi_j \approx 0.77$ instead of ≈ 0.66) seems to indicate that the microstructure of the suspension of apparent particles differs from that of rigid frictionless particles. In turn, this seems to indicate that our second assumption (at page 11) is incorrect. To verify that this is the case, we can consider the density of the particle network, to have a sense of how far the suspension is from jamming. This could be done visually, as in Fig. 4, but the result would be hard to quantify. Instead, we use the *inhomogeneity index*, a quantity defined as follows⁴⁴:

$$I \equiv \frac{\sqrt{\langle [\phi - \langle \phi \rangle]^2 \rangle}}{\langle \phi \rangle} \quad (60)$$

with $\langle \phi \rangle$ denoting the mean value of the solid volume fraction field. The inhomogeneity index has been used to characterize different flow regimes in rheological problems, such as those involving bubbling fluidized beds. Here, we use it as an indication of differences or changes in the microstructure of the

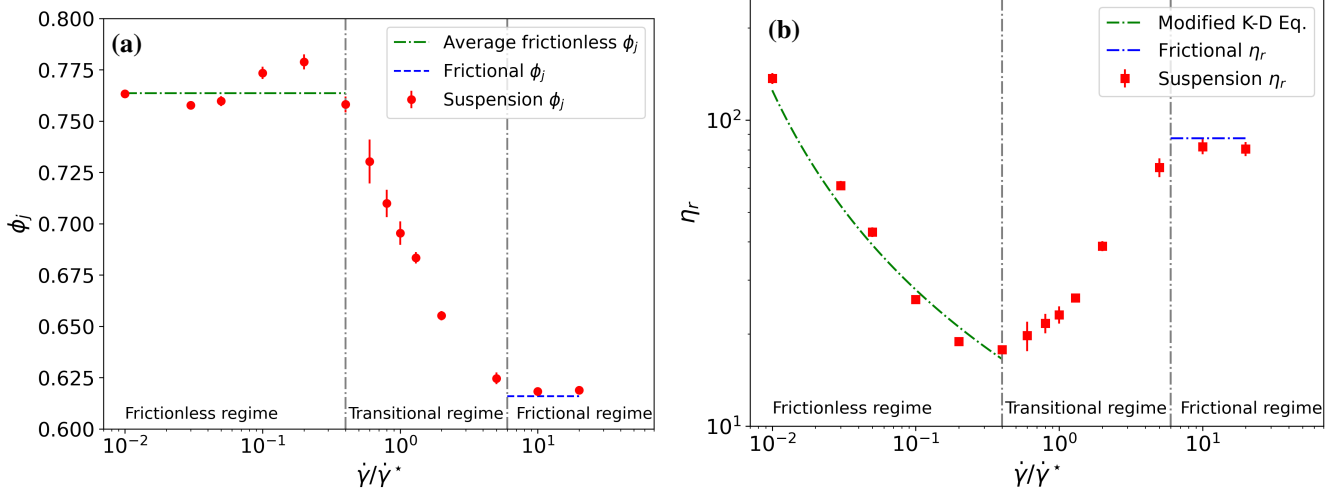


FIG. 8: (a) Apparent jamming volume fraction as a function of the dimensionless shear rate (marked with red circles) for a suspension of repulsive particles with $\phi = 0.55$ and $\kappa^{-1} = 0.05a$. The gray dotted lines mark the frictionless, transitional and frictional regimes. The green dotted line marks the average value of ϕ_j in the frictionless regime, and the blue dotted line marks the value of ϕ_j obtained from Fig. 3. (b) Relative viscosity as a function of the dimensionless shear rate. The suspension viscosity is marked by red squares, and the green dotted line is the plot of the modified Krieger-Dougherty equation (Eq. 58) with ϕ_j^* given by Eq. 57 with $\phi_j = 0.77$. ϕ_j is obtained from the average value in the frictionless regime from Fig. 8a. The blue dotted line represents the viscosity of rigid frictional particles (obtained for $\dot{\gamma}/\dot{\gamma}^* \gg 1$) with $\phi = 0.55$.

suspension. For instance, suspensions of frictionless and frictional rigid non-repulsive particles have different microstructure (see Fig. 4), and this is reflected by a different value of the inhomogeneity index, equal to 0.0526 and 0.0577 (independent of the shear rate) for the two suspensions, respectively. Typically the values lie between 0 and 1⁴⁵; a value of 0 indicates a uniform microstructure, while higher values of I suggest increasing levels of microstructure inhomogeneity. If the inhomogeneity index is constant over a range of $\dot{\gamma}/\dot{\gamma}^*$, we assume that the microstructure is stable, while if it changes over a range of $\dot{\gamma}/\dot{\gamma}^*$, we assume that the microstructure is changing. If our second assumption (at page 11) were correct – that is, if suspensions of rigid non-repulsive frictionless particles and suspensions of apparent frictionless particles had similar microstructure – then, these two types of suspensions should also have a similar value of the inhomogeneity index. Based on the result about the jamming volume fraction ($\phi_j \approx 0.77$ instead of ≈ 0.66), it seems that this assumption may be incorrect. Thus, we now anticipate that these two types of suspensions should have different values of the inhomogeneity index. Fig. 9 shows that the microstructure of the suspension is stable for dimensionless shear rates lower than 0.4 and subsequently gradually becomes more inhomogeneous until the inhomogeneity for the corresponding suspension of rigid non-repulsive frictional particles is fully reached for $\dot{\gamma}/\dot{\gamma}^* \sim 10$. Thus, there is a good correspondence between the apparent jamming volume fraction and the inhomogeneity index (Fig. 8a and Fig. 9). In particular, we observe that the microstructure is stable in the frictionless regime and becomes less uniform as the jamming volume fraction transitions to the frictional regime, where the microstructure reaches a new stable state. This result strengthens the connection between the mi-

crostructure and the jamming volume fraction. However, we note that the suspension of rigid frictionless particles (upper, magenta dashed line in Fig. 9) is more inhomogeneous than the suspension of rigid frictional particles (lower, black dotted line in Fig. 9), while having a larger jamming volume fraction; this indicates that a suspension with a larger jamming volume fraction is not necessarily more homogeneous. Thus, we avoid direct parallels between the values of the inhomogeneity index and of the jamming volume fraction. Since the large value of the inhomogeneity index of frictionless rigid particles is not observed for the suspension of apparent particles, we conclude that the microstructure is different between these two systems. This reveals that we cannot expect the same jamming volume fraction for the two systems. This disproves our second assumption presented at page 11.

We can conclude that the modified Krieger-Dougherty equation results in a good match with the viscosity in the frictionless regime and we have identified a transitional regime where the apparent jamming volume fraction and microstructure gradually transition from those associated with apparent particles to those of rigid non-repulsive frictional particles. The inhomogeneity index of the apparent particles indicates that the obtained apparent jamming volume fraction in the frictionless regime truly exceeds that of the rigid non-repulsive frictionless particles and that these two systems do not behave similarly, and in particular do not have a similar microstructure.

To understand why the systems of rigid and apparent particles behave differently, we scrutinize the particle pair force balance in Eq. 55. At page 11, a part of our first assumption was that the apparent particles, of radius $a + H/2$, do not overlap. We have verified that this assumption is roughly correct,

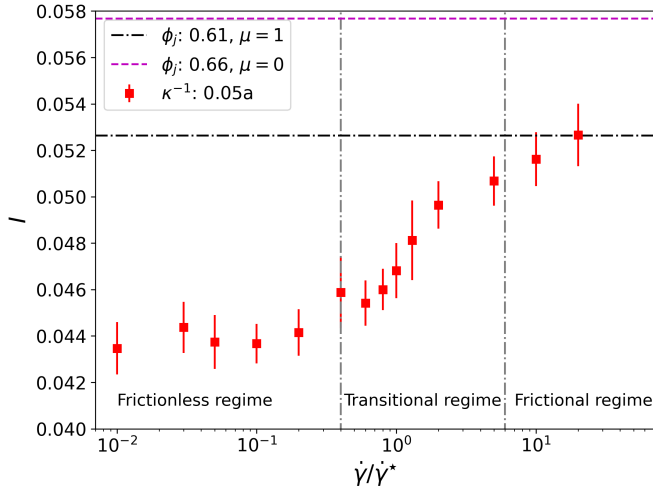


FIG. 9: Inhomogeneity index (Eq. 60) as a function of the dimensionless shear rate for a suspension of repulsive particles with $\phi = 0.55$ and $\kappa^{-1} = 0.05a$. The (lower) black dotted line and the (upper) magenta dashed line mark the inhomogeneity index for the suspensions of non-repulsive frictional and non-repulsive frictionless particles, respectively; both suspensions have $\phi = 0.55$ and the inhomogeneity index is independent of the shear rate. The frictionless, transitional and frictional regimes are distinguished by vertical gray dotted lines.

but this does not mean that there is no overlap present. Being soft, some apparent particles do slightly overlap (as Figs. 6 and 7 indicate). These minor overlaps imply that the particle pairs involved are slightly out of equilibrium and are subjected to a repulsive force that resembles, and can be expressed as, a linear elastic force generated at contact. Like any linear elastic force, this force can be expressed as the product of a spring coefficient and the particle overlap. If the spring coefficient characterizing the apparent particles is much smaller than the spring coefficient of the rigid non-repulsive frictionless particles, then, even if the overlaps are larger for the apparent particles, the contact forces in the network of apparent particles can be far weaker than the contact forces in the network of rigid non-repulsive frictionless particles. The contact forces in the particle network yield its ability to resist the flow, hence weak contact forces increase the ability of the particle network to deform and accommodate more particles. As a consequence, the jamming volume fraction is expected to be significantly larger for the suspension of apparent particles.

To prove this to be the case, we now intend to estimate the spring coefficient for the apparent particles and show that the elastic force is always smaller than that for rigid particles, even if the overlaps for the apparent particles are larger. The corresponding contact force for the apparent particles when their overlap is equal to $\zeta = H - h$, where h is the surface-to-surface particle distance, can be found by expanding the repulsive force around the equilibrium distance H (to the first order) and subtracting the drag force associated with H , which

equals the repulsive force at $h = H$:

$$\begin{aligned} F^{ac}(\zeta) &\approx F_0 e^{-(H-\delta)\kappa} + \kappa F_0 e^{-(H-\delta)\kappa} \zeta - F_d \\ &= \kappa F_0 e^{-(H-\delta)\kappa} \zeta = \kappa F_d \zeta \end{aligned} \quad (61)$$

with $F_d = 6\pi\eta_e a^2 \dot{\gamma} \varepsilon^{-3.70}$. Note the similarity to Hooke's law, which states that the overlap is proportional to the force:

$$F^c(\zeta) = k^n \zeta \quad (62)$$

Therefore, κF_d can be regarded as the normal spring coefficient of the apparent particles. Given a Debye length of $0.05a$, and with the values of the parameters reported in Table I, the apparent spring coefficient is four orders of magnitudes smaller than the spring coefficient k^n of real rigid particles.

Usually, we expect that the value of the spring coefficient does not significantly affect the rheology. This is because a smaller spring coefficient is compensated by a greater particle overlap, yielding the same contact force. To verify that the network formed by the apparent particles is truly weaker than that formed by rigid frictionless particles of equal size, we must take into account the overlap. The overlap between apparent particles required to yield an equal contact force to that between rigid frictionless particles is given by:

$$\zeta_a = \frac{k^n \zeta_r}{\kappa F_d} \quad (63)$$

where ζ_a and ζ_r are the overlaps of the apparent and real particles, respectively. Setting $\zeta_r = 0.04a$ (a value that, somewhat arbitrarily, is regarded as the maximum overlap for rigid particles²⁶) and using the “real” rigid spring coefficient value for k^n , the value of ζ_a given by Eq. 63 is always considerably larger than the added radius of $H/2$. Even if ζ_r is chosen differently, and also considering that for large overlaps Eq. 61 is less precise, we still conclude that the forces associated with the network of apparent particles are considerably weaker than those for real particles.

This indicates that, as expected, the apparent contact forces are significantly weaker than the contact forces in a network of rigid frictionless particles. Hence, we expect the suspension of apparent particles to have a microstructure associated with a larger apparent jamming volume fraction than the jamming volume fraction of a suspension of rigid frictionless particles. Although the value of $\phi_j = 0.77$ for the apparent particle suspension is very large, this system has a large Debye length, which according to Eq. 61 is inversely proportional to the strength of the apparent particle network, hence we expect a large jamming volume fraction.

C. Influence of the Debye length on the rheology

In this section, we consider four repulsive suspensions of a solid volume fraction of 0.55 with Debye lengths of $0.0005a$, $0.005a$, $0.025a$ and $0.05a$.

In Fig. 10a, for $\dot{\gamma}/\dot{\gamma}^* \lesssim 0.4$, we see that the shear-thinning is very well predicted by the modified Krieger-Dougherty

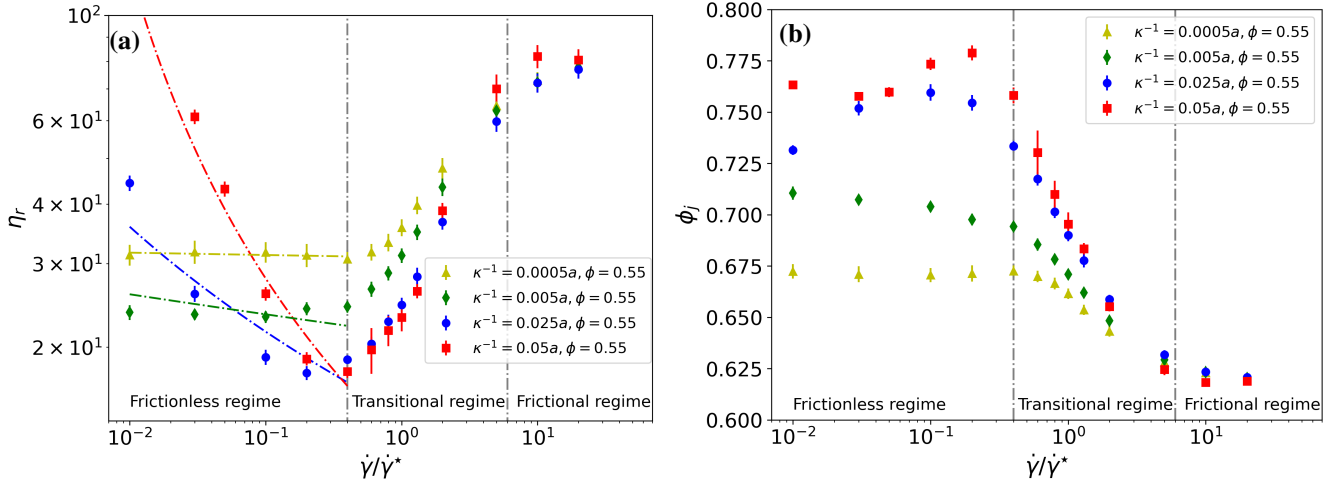


FIG. 10: (a) Relative viscosity as a function of the dimensionless shear rate for suspensions with a solid volume fraction of $\phi = 0.55$ and with κ^{-1} of $0.0005a$, $0.005a$, $0.025a$ and $0.05a$ in yellow triangle, green diamond, blue circle and red square, respectively. The colored dotted lines are the plots of the modified Krieger-Dougherty equation 58 with $C = 1$ and $\lambda = 2.0$ for each case, using the apparent jamming volume fractions of 0.67, 0.70, 0.75 and 0.77 for κ^{-1} equal to $0.0005a$, $0.005a$, $0.025a$ and $0.05a$, respectively. (b) Corresponding apparent jamming volume fraction ϕ_j (Eq. 57) calculated using the viscosity values in Fig. 10a and H from Eq. 56. In both figures the frictionless, transitional and frictional regimes are marked by vertical dotted gray lines with same borders as the base case.

equation (Eq. 58) marked with dotted lines; larger Debye lengths yield a steeper shear-thinning, since H increases more rapidly as the dimensionless shear rate decreases (see Eq. 56). Like the base case, all the suspensions are frictionless when $\dot{\gamma}/\dot{\gamma}^* < 0.4$, where the contact viscosity remains insignificant. As the dimensionless shear rate surpasses unity and the number of particles in direct contact increases, the viscosity values converge during shear-thickening, regardless of the Debye length value. Thus, the rheological behaviors of the suspensions in the frictionless, transitional and frictional regimes are similar to those in the base case.

In Fig. 10b, we note that, in the frictionless regime, the apparent jamming volume fractions are larger than 0.66, the value of the jamming volume fraction of the rigid frictionless particles. Suspensions with larger Debye length values exhibit increasingly larger apparent jamming volume fractions.

To verify that the assumptions stated in the previous section hold true and study how the jamming volume fraction is related to the Debye length, we follow the same procedure adopted for the base case, starting by analyzing H using the histograms of the surface-to-surface distances in the frictionless regime.

In Figs. 11, the x-axis is normalized by the equilibrium distances for the four Debye lengths and the y-axis is normalized by the maximum value of the histogram for the four cases, allowing for comparison. The colored vertical lines indicate the weighted mean distances (Eq. 59); if these occur at a surface-to-surface particle distance $h/H < 1$, this suggests that the apparent particles are overlapping. In Figs. 11, we present the surface-to-surface distribution histograms for the suspension with $\phi = 0.55$ in the frictionless regime. The particle density around the peaks varies significantly across the four

cases, with more particles closely centered around the equilibrium distance for smaller Debye lengths. To facilitate comparison, the surface-to-surface histograms are normalized. For the suspensions with $\kappa^{-1} = 0.0005a$ and $\kappa^{-1} = 0.005a$, the peaks of the distributions and the weighted mean distance (\bar{h}) slightly differ. This is expected, because the weighted mean distance essentially disregards particle pairs whose repulsive interaction force is very weak and because, for these small values of κ^{-1} , the decay of the repulsive force with distance is very rapid; particle pairs falling in the high end of the distribution (i.e., where h is large) do interact very weakly and are thus effectively disregarded, shifting the weighted mean distance to a smaller value compared to the peak of the surface-to-surface distribution. From Figs. 11, we conclude that although the apparent particles overlap, the weighted mean distances (\bar{h}) marked with the vertical lines are of the same order of magnitude as the equilibrium distances ($h/H = 1$) for all the suspensions. Thus, as for the base case, the high values of ϕ_j cannot be explained by an inaccurate estimation of H .

To explore whether we observe a relationship between the microstructure and the apparent jamming volume fraction similar to that in the base case, we analyze the inhomogeneity index in Fig. 12. As we see, the microstructure behaves similarly to the base case. Specifically, the inhomogeneity index is stable in the frictionless regime and then proceeds to change in the transitional regime, where the number of particles in direct contact increases, and stabilizes at a plateau value in the frictional regime. This indicates that the microstructure does not change in the frictionless and frictional regimes, so that in these regimes the apparent jamming volume fraction is constant. In the transitional regime, the inhomogeneity index changes (increasing or decreasing, depending on the value of

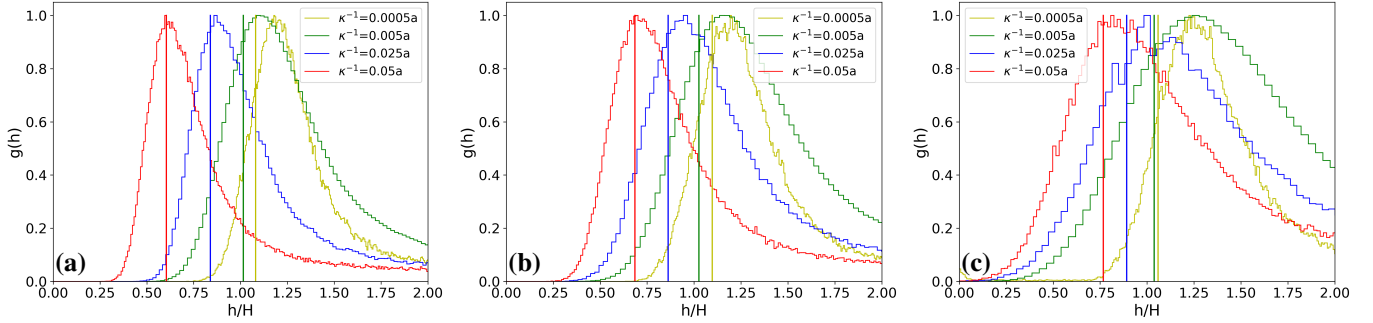


FIG. 11: Normalized surface-to-surface distribution histogram ($g(h)$) for suspensions of repulsive particles with $\phi = 0.55$ and the Debye length values reported in the legend. The surface-to-surface particle distances (h) are normalized by the equilibrium distance H (calculated for every value of the Debye length). The normalized weighted mean distances (\bar{h}/H) are marked by vertical lines. (a) $\dot{\gamma}/\dot{\gamma}^* = 0.01$, (b) $\dot{\gamma}/\dot{\gamma}^* = 0.03$, (c) $\dot{\gamma}/\dot{\gamma}^* = 0.1$.

the Debye length), thus indicating that the particle network changes microstructure. Note that the inhomogeneity index for $\kappa^{-1} = 0.0005a$ is much larger than the inhomogeneity index for rigid frictionless particles, although these two systems have a similar jamming volume fraction and the inhomogeneity index for $\kappa^{-1} = 0.005a$ is similar to rigid frictional particles, although we expect these two systems to have different microstructures. This confirms that the inhomogeneity index characterizes the microstructure but is not directly related to the jamming volume fraction.

We conclude that the microstructures are stable in the

frictionless regime, subsequently change in the transitional regime and stabilize again in the frictional regime, a behavior that is similar to that of the apparent jamming volume fraction in Fig. 10b. The microstructures are not only a function of the dimensionless shear rate but also of the value of the Debye length, a behavior that is also found for the apparent jamming volume fraction.

To understand how the Debye length affects the jamming volume fraction, we use the equation for the apparent spring coefficient (Eq. 61). It gives us an estimate of the strength of the forces associated with the particle network, hence an indication of the relative value of the apparent jamming volume fraction. Since the apparent spring coefficient is inversely proportional to the Debye length, the particle network strength is two orders of magnitude larger for the suspension with the smallest Debye length ($\kappa^{-1} = 0.0005a$) than that for the suspension with the largest Debye length ($\kappa^{-1} = 0.05a$). Thus, Fig. 10b shows the expected behavior, where the apparent jamming volume fraction increases with the Debye length. The limiting range of ϕ_j is between 0.66 and 0.8; the lower bound is given by the jamming volume fraction of rigid frictionless particles and the upper bound by a suspension with a microstructure with a regular crystal arrangement for particles with a radii ratio of 1:1.4. Although we cannot relate the apparent spring coefficient to a specific jamming volume fraction, the apparent jamming volume fraction of the suspension with the smallest Debye length is close to that of rigid frictionless particles, (0.67 and 0.66, respectively), while for the suspension with the largest Debye length, ϕ_j is close to the upper bound (0.77 and 0.8, respectively). These results suggest that a suspension of repulsive particles with an apparent spring coefficient of about 1 N/m (using Eq. 61 with $\kappa^{-1} = 0.0005a$) has a particle network strength similar to that of a non-repulsive frictionless particle suspension with the same volume fraction, while a suspension of repulsive particles with an apparent spring coefficient of about 10^{-2} N/m (using Eq. 61 with $\kappa^{-1} = 0.05a$) has a significantly weaker particle network that allows the particles to move almost unhindered, allowing a large jamming volume fraction.

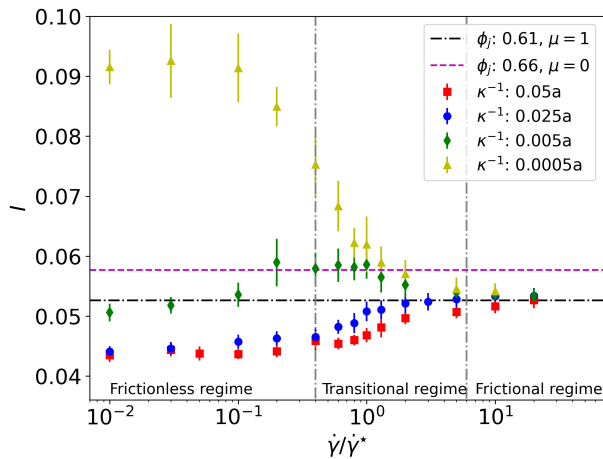


FIG. 12: Inhomogeneity index (Eq. 60) as a function of the dimensionless shear rate for suspensions with different Debye lengths (according to the legend) and suspensions of rigid frictional and frictionless particles with $\phi = 0.55$. The (lower) black and (upper) magenta dotted lines mark the inhomogeneity index for the non-repulsive frictional and non-repulsive frictionless suspensions, respectively (see Fig. 3). The values of the jamming volume fractions of the non-repulsive suspensions are shown in the legend for reference. The frictionless, transitional and frictional regimes are marked by vertical dotted gray lines.

VII. CONCLUSIONS

We have developed a comprehensive and rigorous model for simulating suspensions within the CFD-DEM framework, incorporating relevant fluid and interparticle interactions. This model allows analyzing the stress contributions in sheared suspensions with medium to large solid volume fractions and any short-ranged interparticle potentials. Given that these systems are overdamped, we introduced a new time step criterion to account for lubrication forces, as the traditional Belytschko's criterion is insufficient.

We used this model to study the rheology of suspensions of neutrally buoyant, non-Brownian, repulsive particles under conditions of low particle and fluid inertia ($St < 1$, $Re < 1$). We performed simulations at a solid volume fraction of 55% and Debye lengths ranging from 0.0005 to 0.05 particle radii, involving approximately 40,000 particles.

The results confirm that our definition of characteristic shear rate ($\dot{\gamma}^*$) accurately predicts the onset of shear-thickening at the expected order of magnitude of the dimensionless shear rate. We have identified three regimes: a frictionless regime, where no contacts are present between the solid particles and the microstructure of the suspension is stable; a transitional regime, where frictional contacts start forming between the particles, the microstructure of the suspension changes progressively, and the jamming volume fraction shifts from the values associated with suspensions of repulsive frictionless particles to those associated with suspensions of non-repulsive frictional particles; and a frictional regime, where direct particle contacts dominate, yielding the behavior of suspensions of non-repulsive frictional particles. In the frictionless regime, our modified Krieger-Dougherty equation accurately describes the shear-thinning behavior. Notably, the systems of apparent particles, having a rigid core surrounded by a “soft” liquid shell, exhibited an apparent jamming volume fraction that increased with the Debye length.

To explain the behavior of the apparent jamming volume fraction, we derived an expression for the spring coefficient for the apparent particles. Since this coefficient, as well as the overlaps between the apparent particles, is considerably small, the resulting force network within the suspension is rather weak, leading to a relative small resistance to the flow of the suspension and in turn to an increased ability of the particle network to deform, which ultimately results into a larger value of the jamming volume fraction. Since the apparent spring coefficient is inversely proportional to the Debye length, larger Debye lengths yield weaker particle networks and therefore larger apparent jamming volume fractions.

ACKNOWLEDGMENTS

We wish to acknowledge Johnson Matthey PLC for the financial support given to this project.

DECLARATION OF COMPETING INTEREST

The authors declare that they have no known competing financial interests or personal relationships that could have appeared to influence the work reported in this paper.

DATA AVAILABILITY STATEMENT

Data will be made available on request.

Appendix A: Time step

A widely adopted criterion for selecting DEM time steps, called the Belytschko criterion, is given by $\Delta t_c = \sqrt{m/k^n}$ ⁴⁶. This criterion is commonly used for granular systems. But its validity for overdamped systems, such as particles immersed in a fluid, is questionable, because overdamped systems lack a natural angular frequency – the presence of this frequency being a key assumption in the Belytschko method. Therefore, for overdamped systems, we employ the amplification matrix method⁴⁷. We start by deriving the Belytschko criterion to show what conditions must be satisfied for it to apply, then we derive a new time step criterion, and finally we compare the two criteria to highlight for what spring coefficient values our time step criterion must be used.

Absence of fluid-particle interactions

The equation of motion in the normal direction for a sphere involved in a linear viscoelastic collision with another identical particle reads:

$$m\ddot{x} = -\eta^n \dot{x} - k^n x \quad (\text{A1})$$

where x is the position of the particle relative to the other particle, η^n is the normal damping coefficient and k^n is the normal spring coefficient. Eq. A1 is the equation of a damped harmonic oscillator; rearranging it in terms of its frequency and damping coefficient yields:

$$\ddot{x} + 2\psi\dot{x} + \kappa_0^2 x = 0 \quad (\text{A2})$$

with:

$$\psi \equiv \frac{\eta^n}{2m} \quad ; \quad \kappa_0^2 \equiv \frac{k^n}{m} \quad (\text{A3})$$

where κ_0 is the frequency of the undamped harmonic oscillator and ψ is the reduced damping coefficient. Eq. A2 can be solved analytically with initial conditions $x(0) = 0$ and $\dot{x}(0) = v_0$, where v_0 is the normal relative particle impact velocity. The solution is:

$$\dot{x}(t) = \frac{v_0}{\omega} e^{-\psi t} \sin(\omega t) \quad (\text{A4})$$

$$x(t) = \frac{v_0}{\omega} e^{-\psi t} [\omega \cos(\omega t) - \psi \sin(\omega t)] \quad (\text{A5})$$

with $\omega \equiv \sqrt{\kappa_0^2 - \psi^2}$ denoting the natural angular frequency. For an explicit finite element method analysis, Belytschko expressed the critical time step as⁴⁷:

$$\Delta t_c = \frac{2}{\omega} \quad (\text{A6})$$

Expressing this equation in terms of the parameters featuring in Eq. A1 yields:

$$\Delta t_c = \frac{2}{\sqrt{\frac{k^n}{m} - \left(\frac{\eta^n}{2m}\right)^2}} \quad (\text{A7})$$

The time criterion of Eq. A7 is smallest when $\eta^n = 0$ and can thus be represented by:

$$\Delta t_c = \sqrt{\frac{m}{k^n}} \quad (\text{A8})$$

which retrieves the time step criterion presented in the introduction. If the system is overdamped (that is, if $\kappa_0^2 < \psi$), Eq. A7 does not have a real solution and cannot be used.

Presence of fluid-particle interactions

For particles immersed in a liquid, we must modify Eq. A1 to consider the lubrication and drag forces. At contact, it is customary to fix the interparticle distance of the lubrication force to the surface roughness; thus, we write:

$$\begin{aligned} m\ddot{x} = & -[\eta^n + 6\pi\eta_e a \varepsilon^{-3.70} + (3/2)\pi a^2 \eta_e / \delta] \dot{x} \\ & - k^n x + 6\pi\eta_e a^2 \dot{\gamma} \varepsilon^{-3.70} \end{aligned} \quad (\text{A9})$$

where η_e , a and ε are the fluid viscosity, particle radius and fluid volume fraction, respectively. Given a surface roughness of $\delta \sim 0.001a$, the lubrication force is the leading term of the damping in Eq. A9. By repeating the steps in the previous section, we obtain the natural angular frequency:

$$\omega = \sqrt{\frac{k^n}{m} - \left[\frac{(3/2)\pi a^2 \eta_e / \delta}{m}\right]^2} \quad (\text{A10})$$

For Eq. A10 to have a real solution, k^n must be larger than $\sim 2000 \text{ N/m}$, for $a = 5 \mu\text{m}$, $\eta_e = 0.001 \text{ Pa}\cdot\text{s}$ and $\rho = 1000 \text{ kg/m}^3$, so that the system is underdamped. This value of k^n is larger than what is sometimes used in the literature⁴⁸. Hence, we proceed to derive a time step criterion that does not require the system to be underdamped.

Amplification matrix method

The most common integrator scheme used by DEM software is the velocity Verlet integrator (used by LIGGGHTS and LAMMPS). The default velocity Verlet algorithm as used by LAMMPS and LIGGGHTS is the following:

$$1. \dot{\mathbf{x}}_{n+(1/2)} = \dot{\mathbf{x}}_n + (\Delta t/2) \ddot{\mathbf{x}}_n$$

$$2. \mathbf{x}_{n+1} = \mathbf{x}_n + \Delta t \dot{\mathbf{x}}_{n+(1/2)}$$

$$3. \ddot{\mathbf{x}}_{n+1} = \mathbf{F}/m = C \dot{\mathbf{x}}_{n+(1/2)} + k \mathbf{x}_{n+1} + \mathbf{f}/m$$

$$4. \dot{\mathbf{x}}_{n+1} = \dot{\mathbf{x}}_{n+(1/2)} + (\Delta t/2) \ddot{\mathbf{x}}_{n+1}$$

with:

$$C \equiv -\frac{(3/2)\pi a^2 \eta_e / \delta}{m}; \quad k \equiv -\frac{k^n}{m} \quad (\text{A11})$$

where C is related to the lubrication force (see the first term on the right-hand side of Eq. A9, where, as done previously, the first two terms in square brackets have been neglected), k is related to the contact force (the second term on the right-hand side of Eq. A9) and \mathbf{f} represents additional forces unrelated to the particle position and velocity (such as the last term on the right-hand side of Eq. A9). Step 3 updates the acceleration considering the total force \mathbf{F} . Note that the forces are updated using the half time step velocity.

Let us rearrange the equations in steps 1 to 4 to express the updated variables in terms of the variables of the previous time step and simplify to one dimension:

$$\mathbf{d} = \mathbf{Ab} + \mathbf{c} \quad (\text{A12})$$

with:

$$\mathbf{A} \equiv \begin{bmatrix} 0 & 0 & \frac{\Delta t}{2} & 1 \\ 0 & 1 & \frac{\Delta t^2}{2} & \Delta t \\ 0 & k & \frac{k\Delta t^2}{2} + \frac{C\Delta t}{2} & k\Delta t + C \\ 0 & \frac{k\Delta t}{2} & \frac{\Delta t}{2}(1 + C\frac{\Delta t}{2} + \frac{k\Delta t^2}{2}) & 1 + \frac{\Delta t}{2}(C + k\Delta t) \end{bmatrix}$$

$$\mathbf{b} \equiv \begin{bmatrix} 0 \\ \mathbf{x}_n \\ \ddot{\mathbf{x}}_n \\ \dot{\mathbf{x}}_n \end{bmatrix}; \quad \mathbf{c} \equiv \begin{bmatrix} 0 \\ 0 \\ \mathbf{f}/m \\ 0 \end{bmatrix}; \quad \mathbf{d} \equiv \begin{bmatrix} \dot{\mathbf{x}}_{n+(1/2)} \\ \mathbf{x}_{n+1} \\ \ddot{\mathbf{x}}_{n+1} \\ \dot{\mathbf{x}}_{n+1} \end{bmatrix} \quad (\text{A13})$$

\mathbf{A} is referred to as amplification matrix. For stability, its maximum absolute eigenvalue must be less than unity; this gives a condition for the maximum stable time step.

Calculating the eigenvalues of the amplification matrix is complex, so we have used Python and the library “SymPy”. The eigenvalues are:

$$\begin{aligned} \lambda_1 &= \frac{C\Delta t + \Delta t^2 k}{2} \\ &+ \frac{\Delta t}{2} \sqrt{C^2 + 2C\Delta t k + \Delta t^2 k^2 + 4k} + 1 \end{aligned} \quad (\text{A14})$$

$$\begin{aligned} \lambda_2 &= \frac{C\Delta t + \Delta t^2 k}{2} \\ &- \frac{\Delta t}{2} \sqrt{C^2 + 2C\Delta t k + \Delta t^2 k^2 + 4k} + 1 \end{aligned} \quad (\text{A15})$$

$$\lambda_3 = 0; \quad \lambda_4 = 0 \quad (\text{A16})$$

Using SymPy, we take the absolute values of λ_1 and λ_2 , set them equal to unity and solve for Δt . For both eigenvalues, we obtain the following critical time step:

$$\Delta t_c = \frac{-C \pm \sqrt{C^2 - 4k}}{k} \quad (\text{A17})$$

In Eq. A17, the negative sign (for the square root term) yields the only positive time step. This critical value is equivalent to that derived for the Euler integrator⁴⁷. In an undamped system ($C = 0$), we roughly retrieve Belytschko's time criterion:

$$\Delta t_c = \sqrt{\frac{2m}{k^n}} \quad (\text{A18})$$

Let us express Eq. A17 in terms of the lubrication force and spring stiffness:

$$\Delta t_c = \frac{(3/2)\pi a^2 \eta_e / \delta}{k^n} - \frac{\sqrt{[(3/2)\pi a^2 \eta_e / \delta]^2 - 4mk^n}}{k^n} \quad (\text{A19})$$

In Fig. 13, we compare the Belytschko time step criterion (Eq. A8) with our (overdamped) time step criterion (Eq. A19) as a function of the normal spring coefficient (k^n). From Fig.

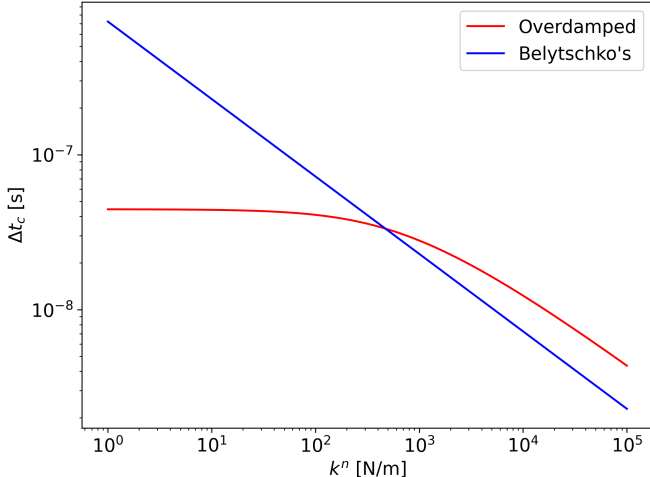


FIG. 13: Belytschko's time step criterion (blue line); new time step criterion for overdamped systems (red line). $a = 5 \mu\text{m}$, $\delta = 0.001a$, $\eta_e = 0.001 \text{ Pa}\cdot\text{s}$ and $\rho = 1000 \text{ kg}/\text{m}^3$.

13, we note that the Belytschko criterion highly overestimates the critical time step for small spring coefficients. The graph indicates that a spring coefficient less than $\sim 10^2 \text{ N/m}$ is unnecessary, since it does not result into a larger value of the critical time step. It is generally good to have a large spring coefficient to avoid largely overlapping particles, but this requires a smaller time step.

Appendix B: Shear rate scale

Over the past decade, the prevailing notion has been that the onset of shear thickening or the transition from frictionless to frictional rheology is characterized by an “onset stress” with a weak dependence on ϕ , while the “onset shear rate” changes with ϕ more strongly⁴⁹. Consequently, it has been common to discuss the onset of shear thickening in terms of stress, using the stress scale. But as demonstrated in Fig. 2, the onset shear rate is largely independent of ϕ . The marked dependence of the onset shear rate on ϕ stems from the classical definition of the drag force scale, taken to be equal to $6\pi\eta_e a^2 \dot{\gamma}$. This scale is correct only for very dilute suspensions. To estimate the shear rate scale, we must prove Eq. 54, because from this equation the definition of $\dot{\gamma}^*$ follows. Let us start from the general linear momentum balance equation for particle r interacting with particle s :

$$m\dot{\mathbf{u}}_r = \mathbf{f}_{d,r} + \mathbf{f}_{b,r} + \mathbf{f}_{rs}^\bullet + \mathbf{f}_{rs}^c + \mathbf{f}_{rs}^i + mg \quad (\text{B1})$$

where $\mathbf{f}_{b,r}$ is the buoyancy force. We assume a low Reynolds number and neutrally buoyant particles; then, the Stokes and Reynolds numbers are equal, and the inertia of the particles is negligible. For simplicity, here we define the buoyancy force according to the Archimedes principle (this is convenient, because, for neutrally buoyant particles, the buoyancy force and the weight force balance each other). As this definition differs from that employed in the main article, we must modify the closure for the drag force, to ensure that the total fluid-particle interaction force is modeled correctly³⁵. The drag force based on the Archimedes definition of the buoyancy force, denoted as $\mathbf{f}_{d,r}^A$, is related to the drag force adopted in the main article by the equation $\mathbf{f}_{d,r}^A = \mathbf{f}_{d,r}/\varepsilon$. As we consider particles r and s approaching, we can disregard the contact force \mathbf{f}_{rs}^c . Thus, we can write:

$$\mathbf{f}_{d,r}^A + \mathbf{f}_{rs}^\bullet + \mathbf{f}_{rs}^i + V_p(\rho_p - \rho_e)\mathbf{g} = \mathbf{0} \quad (\text{B2})$$

where ρ_p is the density of particle r . Since we are considering neutrally buoyant particles, the last term in Eq. B2 vanishes. Thus, Eq. B2 reduces to:

$$\mathbf{f}_{d,r}^A = -\mathbf{f}_{rs}^\bullet - \mathbf{f}_{rs}^i \quad (\text{B3})$$

In terms of orders of magnitude, we have:

$$|\mathbf{f}_{rs}^\bullet| \sim (3/2)\pi a^2 \eta_e (v/h) \quad ; \quad |\mathbf{f}_{rs}^i| \sim F_0 e^{-(h-\delta)\kappa} \quad (\text{B4})$$

For the drag force, since we are considering a low Reynolds number, in Eq. 19 we set $\alpha = 3.7$ and $C_D = 4.8^2/\text{Re}$. Thus, Eq. 17 yields:

$$|\mathbf{f}_{d,r}^A| \sim \frac{1}{\varepsilon} \left[(\pi a^2) \frac{1}{2} \left(\frac{4.8^2 \eta_e}{2a\varepsilon} \right) \right] \varepsilon^{2-3.7} |\langle \mathbf{u} \rangle_e - \mathbf{u}_r| \quad (\text{B5})$$

But it is:

$$|\langle \mathbf{u} \rangle_e - \mathbf{u}_r| \sim \dot{\gamma}a - v \quad (\text{B6})$$

Therefore, we obtain:

$$|\mathbf{f}_{d,r}^A| \sim 6\pi\eta_e a(\dot{\gamma}a - v)\varepsilon^{-3.70} \quad (\text{B7})$$

Inserting Eqs. B4 and B7 into Eq. B3, we obtain Eq. 54. This leads to Eq. 56 with $\dot{\gamma}^*$ defined as per Eq. 53.

REFERENCES

- ¹D. J. Jeffrey and A. Acrivos, "The rheological properties of suspensions of rigid particles," *AIChE Journal* **22** (1976), 10.1002/aic.690220303.
- ²Y. Zhu, G. Lv, C. Song, B. Li, Y. Zhu, Y. Liu, W. Zhang, and Y. Wang, "Optimization of the washcoat slurry for hydrotalcite-based LNT catalyst," *Catalysts* **9** (2019), 10.3390/catal9080696.
- ³R. Jackson, "Locally averaged equations of motion for a mixture of identical spherical particles and a newtonian fluid," *Chemical Engineering Science* **52**, 2457–2469 (1997).
- ⁴B. Blais and F. Bertrand, "On the use of the method of manufactured solutions for the verification of cfd codes for the volume-averaged navier–stokes equations," *Computers & Fluids* **114**, 121–129 (2015).
- ⁵M. Manninen and V. Taivassalo, *On the mixture model for multiphase flow* (Valtion Teknillinen Tutkimuskeskus, 1996).
- ⁶C. Ness, R. Seto, and R. Mari, "The physics of dense suspensions," *Annual Review of Condensed Matter Physics* **13**, 97–117 (2022).
- ⁷E. DeGiuli, G. Düring, E. Lerner, and M. Wyart, "Unified theory of inertial granular flows and non-brownian suspensions," *Physical Review E* **91**, 062206 (2015).
- ⁸I. M. Krieger and T. J. Dougherty, "A mechanism for non-newtonian flow in suspensions of rigid spheres," *Transactions of The Society of Rheology* **3**, 137–152 (1959).
- ⁹M. Otsuki and H. Hayakawa, "Critical scaling near jamming transition for frictional granular particles," *Physical Review E* **83**, 051301 (2011).
- ¹⁰L. C. Hsiao, S. Jamali, E. Glynnos, P. F. Green, R. G. Larson, and M. J. Solomon, "Rheological state diagrams for rough colloids in shear flow," *Physical Review Letter* **119**, 158001 (2017).
- ¹¹J. A. Richards, B. M. Guy, E. Blanco, M. Hermes, G. Poy, and W. C. K. Poon, "The role of friction in the yielding of adhesive non-brownian suspensions," *Journal of Rheology* **64**, 405–412 (2020).
- ¹²A. Singh, "Hidden hierarchy in the rheology of dense suspensions," *MRS Communications* **13** (2023), 10.1557/s43579-023-00450-2.
- ¹³D. C. GmbH and J. Linz, "CFDEM," (2022).
- ¹⁴C. Ness and J. Sun, "Shear thickening regimes of dense non-brownian suspensions," *Soft Matter* **12**, 914–924 (2016).
- ¹⁵R. Mari, R. Seto, J. F. Morris, and M. M. Denn, "Shear thickening, frictionless and frictional rheologies in non-brownian suspensions," *Journal of Rheology* **58** (2014), 10.1122/1.4890747.
- ¹⁶R. Jamshidi, P. Angeli, and L. Mazzei, "On the closure problem of the effective stress in the eulerian-eulerian and mixture modeling approaches for the simulation of liquid-particle suspensions," *Physics of Fluids* (2019), 10.1063/1.5081677.
- ¹⁷R. Jamshidi, J. J. Gillissen, P. Angeli, and L. Mazzei, "Roles of solid effective stress and fluid-particle interaction force in modeling shear-induced particle migration in non-brownian suspensions," *Physical Review Fluids* **6** (2021), 10.1103/PhysRevFluids.6.014301.
- ¹⁸R. Jackson, *The Dynamics of Fluidized Particles*, Cambridge Monographs on Mechanics (Cambridge University Press, 2000).
- ¹⁹D. J. Jeffrey and Y. Onishi, "Calculation of the resistance and mobility functions for two unequal rigid spheres in low-reynolds-number flow," *Journal of Fluid Mechanics* **139**, 261–290 (1984).
- ²⁰D. J. Jeffrey, "The calculation of the low Reynolds number resistance functions for two unequal spheres," *Physics of Fluids A: Fluid Dynamics* **4**, 16–29 (1992).
- ²¹O. Cheal and C. Ness, "Rheology of dense granular suspensions under extensional flow," *The Society of Rheology* (2018), 10.1122/1.5004007.
- ²²R. Di Felice, "The voidage function for fluid-particle interaction systems," *International Journal of Multiphase Flow* , 153–159 (1994).
- ²³Y. Liu, Z.-Y. Yin, L. Wang, and Y. Hong, "A coupled CFD–DEM investigation of internal erosion considering suspension flow," *Canadian Geotechnical Journal* **58**, 1411–1425 (2021).
- ²⁴S. Bnà, R. Ponzini, M. Cestari, C. Cavazzoni, C. Cottini, and A. Benassi, "Investigation of particle dynamics and classification mechanism in a spiral jet mill through computational fluid dynamics and discrete element methods," *Powder Technology* **364**, 746–773 (2020).
- ²⁵P. D. Cundall and O. D. L. Strack, "A discrete numerical model for granular assemblies," *Geotechnique* (1979), 10.1680/geot.1979.29.1.47.
- ²⁶H. R. Norouzi, R. Zarghami, R. Sotudeh-Gharebagh, and N. Mostofi, *Coupled CFD-DEM Modeling* (WILEY, 2016).
- ²⁷D. C. GmbH and J. Linz, "LIGGGHTS," (2022).
- ²⁸R. G. Horn, "Surface forces and their action in ceramic materials," *Journal of the American Ceramic Society* **73**, 1117–1135 (1990).
- ²⁹J. Mewis and N. J. Wagner, "Hydrodynamic effects: Non-colloidal particles," (Cambridge University Press, 2011) p. 36–79, 10.1017/CBO9780511977978.005.
- ³⁰G. Chatté, J. Comtet, A. Niguès, L. Bocquet, A. Siria, G. Ducourret, F. Lequeux, N. Lenoir, G. Ovarlez, and A. Colin, "Shear thinning in non-brownian suspensions," *Soft Matter* **14**, 879–893 (2018).
- ³¹D. Joseph, D. Saville, T. Lundgren, and R. Jackson, "Ensemble averaged and mixture theory equations for incompressible fluid-particle suspensions," *International Journal of Multiphase Flow* , 35–42 (1990).
- ³²S. Mueller, E. W. Llewellyn, and H. M. Mader, "The rheology of suspensions of solid particles," *Proceedings of the Royal Society A* **466** (2010), 10.1098/rspa.2009.0445.
- ³³G. K. Batchelor and J. T. Green, "The determination of the bulk stress in a suspension of spherical particles to order c^2 ," *Journal of Fluid Mechanics* **56**, 401–427 (1972).
- ³⁴D. Bedaux, "The effective viscosity for a suspension of spheres," *Journal of Colloid and Interface Science* **118**, 80–86 (1987).
- ³⁵L. Mazzei, "Recent advances in modeling gas-particle flows," in *Handbook of Multiphase Flow Science and Technology*, edited by G. H. Yeoh (Springer Singapore, Singapore, 2017) pp. 1–43.
- ³⁶C. S. O'Hern, L. E. Silbert, A. J. Liu, and S. R. Nagel, "Jamming at zero temperature and zero applied stress: The epitome of disorder," *Physical Review E* **68**, 011306 (2003).
- ³⁷A. Einstein, "Eine neue bestimmung der moleküldimensionen," *Annalen der Physik* **324**, 289–306 (1906).
- ³⁸D. De Laat, F. M. De Oliveira Filho, and F. Vallentin, "Upper bounds for packings of spheres of several radii," *Forum of Mathematics, Sigma* **2** (2014), 10.1017/fms.2014.24.
- ³⁹Y. Forterre and O. Pouliquen, "Flows of dense granular media," *Annual Review of Fluid Mechanics* **40**, 1–24 (2008).
- ⁴⁰M. Wyart and M. E. Cates, "Discontinuous shear thickening without inertia in dense non-brownian suspensions," *Physical Review Letter* **112** (2014), 10.1103/PhysRevLett.112.098302.
- ⁴¹F. m. c. Boyer, E. Guazzelli, and O. Pouliquen, "Unifying suspension and granular rheology," *Physical Review Letter* **107**, 188301 (2011).
- ⁴²C. Ness and J. Sun, "Flow regime transitions in dense non-brownian suspensions: Rheology, microstructural characterization, and constitutive modeling," *Physical Review E* **91**, 012201 (2015).
- ⁴³I. Zarraga, D. Hill, and D. Leighton, "Normal stresses and free surface deformation in concentrated suspensions of noncolloidal spheres in a viscoelastic fluid," *Journal of Rheology* **45** (2001), 10.1122/1.1396356.
- ⁴⁴Q. Guo, S. Meng, Y. Zhao, L. Ma, D. Wang, M. Ye, W. Yang, and Z. Liu, "Experimental verification of solid-like and fluid-like states in the homogeneous fluidization regime of geldart A particles," *Industrial & Engineering Chemistry Research* **57**, 2670–2686 (2018).
- ⁴⁵A. Ozel, Y. Gu, C. C. Milioli, J. Kolehmainen, and S. Sundaresan, "Towards filtered drag force model for non-cohesive and cohesive particle-gas flows," *Physics of Fluids* **29**, 103308 (2017).
- ⁴⁶T. Belytschko, *An Overview of Semidiscretization and Time Integration Procedures* (North Holland, 1983).
- ⁴⁷D. Peng, S. J. Burns, and K. J. Hanley, "Critical time step for discrete element method simulations of convex particles with central symmetry," *International Journal for Numerical Methods in Engineering* **122**, 919–933 (2021).
- ⁴⁸B. Blais, M. Lassaigne, C. Goniva, L. Fradette, and F. Bertrand, "Development of an unresolved cfd–dem model for the flow of viscous suspensions and its application to solid–liquid mixing," *Journal of Computational Physics* **318**, 201–221 (2016).
- ⁴⁹E. Brown and H. M. Jaeger, "Shear thickening in concentrated suspensions: phenomenology, mechanisms and relations to jamming," *Reports on Progress in Physics* **77**, 046602 (2014).